

ENHANCING THERMAL SUNYAEV-ZEL'DOVICH ANALYSES WITH DIGITAL TWINS OF THE LOCAL UNIVERSE

RICHARD STISKALEK[✉]

Astrophysics, University of Oxford, Denys Wilkinson Building, Keble Road, Oxford, OX1 3RH, UK

HARRY DESMOND[✉]

Institute of Cosmology & Gravitation, University of Portsmouth, Dennis Sciama Building, Portsmouth, PO1 3FX, UK

Version January 23, 2026

Abstract

The thermal Sunyaev–Zel'dovich (tSZ) effect provides a powerful probe of the thermal pressure of ionised gas in galaxy clusters and the cosmic web; constrained simulations reconstruct the mass and velocity fields of the local Universe. We explore how these two may be mutually informative: the tSZ signal provides a benchmark for assessing the fidelity of constrained simulations, and constrained simulations contribute information on the positions, total masses and density profiles of cosmic web structures for use in tSZ studies. We focus on cluster predictions in the *Bayesian Origin Reconstruction from Galaxies* (BORG) paradigm, introducing **CSiBORG-Manticore**, a new state-of-the-art suite of digital twins—data-constrained posterior simulations whose initial conditions are inferred via Bayesian forward modelling. We develop a framework for scoring constrained simulations on their ability to match measured Compton- y maps from *Planck* for cluster cutouts, and use it to demonstrate improvement from previous BORG reconstructions. We further validate halo masses against weak-lensing-calibrated X-ray masses from *eROSITA*. We also show how high-fidelity digital twins offer a practical route to extracting additional information from tSZ data through a novel calibration of the mass-observable relation, and provide a complementary framework to purely statistical analyses of Compton- y maps. This paves the way for integrating the large-scale structure information inherent in constrained simulations into the study of CMB secondary anisotropies.

Subject headings: Thermal Sunyaev–Zel'dovich effect, constrained simulations

1. INTRODUCTION

The thermal Sunyaev–Zel'dovich (tSZ) effect is a premier tool in modern cosmology and cluster astrophysics. It arises from inverse Compton scattering of cosmic microwave background (CMB) photons by hot, ionised electrons, primarily in the intracluster medium of galaxy groups and clusters. This scattering conserves photon number but redistributes photon energies, producing a characteristic spectral distortion of the CMB that is independent of redshift. As a result, the tSZ effect provides a nearly redshift-independent probe of the integrated thermal energy of ionised gas along the line of sight, making it a powerful tracer of the cluster population, large-scale structure and baryonic physics (Sunyaev and Zeldovich 1970, 1972; Mroczkowski *et al.* 2019).

In the context of galaxy clusters, the integrated tSZ signal provides a mass proxy because it traces the total thermal energy of ionised gas bound in the cluster potential well. Observational analyses calibrate this Y –mass relation either empirically by combining tSZ measurements with independent mass estimates (e.g. weak gravitational lensing or X-ray hydrostatic masses) or by fitting external scaling relations based on simulations and multi-wavelength data; the latter includes an implicit “mass

bias” parameter quantifying the ratio of the observable-inferred mass to the true mass (von der Linden *et al.* 2014; Hoekstra *et al.* 2015; Collaboration 2016; Salvati *et al.* 2019). Mass estimates derived from the tSZ signal are then propagated into cluster cosmology analyses of number counts and clustering, and compared to masses obtained from other techniques, enabling assessments of systematic biases and improvements in cosmological parameter constraints (Planck Collaboration *et al.* 2014, 2016a; de Haan *et al.* 2016; Bocquet *et al.* 2019; Hilton *et al.* 2021; Bocquet *et al.* 2024a,b).

Compton- y maps are also used beyond individual cluster masses (Planck Collaboration *et al.* 2016b; Chandran *et al.* 2023; McCarthy and Hill 2024): they constitute a projected tracer of the large-scale electron pressure field, which can be statistically analysed through its auto-power spectrum or cross-correlations with other large-scale structure tracers such as galaxy density or weak gravitational lensing. These cross-correlations measure the joint spatial distribution of baryons and matter, providing independent constraints on astrophysical processes and cosmology (Koukoufilippas *et al.* 2020; Yan *et al.* 2021; Tröster *et al.* 2022; Koukoufilippas *et al.* 2022; La Posta *et al.* 2025). Using such two-point statistics, one can test models of gas thermodynamics and feedback (Battaglia *et al.* 2012a), and relate the tSZ signal to

other mass tracers on cosmic scales, making Compton- y maps a versatile probe in multi-probe analyses of structure formation.

The aim of the paper is to connect the tSZ effect with constrained simulations of the local Universe and develop a framework within which each may be used to inform the other. Constrained simulations offer a complementary approach to standard cosmological simulations by tailoring the simulation volume to the actual local Universe. Rather than sampling a random realisation of Λ -cold dark matter (Λ CDM), these methods aim to reproduce the observed large-scale structure by incorporating data such as galaxy redshift surveys or peculiar velocity measurements into the reconstruction of initial conditions (the phases of the initial density modes). This strategy has enabled detailed studies of the nearby cosmic web, the dynamics of the Local Group, and the properties of prominent clusters and superclusters, while retaining statistical consistency of the underlying cosmological model on unconstrained scales (e.g. Dolag *et al.* 2005; Gottlöber *et al.* 2010; Sorce *et al.* 2016). A state-of-the-art approach to constructing the constraints is Bayesian forward-modelling as encapsulated in the *Bayesian Origin Reconstruction from Galaxies* (BORG) paradigm, which provides a full posterior distribution of initial conditions consistent with the local galaxy number density field (Jasche and Wandelt 2013).

The tSZ effect is a particularly natural observable to combine with constrained simulations, as it directly probes the integrated thermal pressure of ionised gas within the same large-scale structures that constrained reconstructions seek to reproduce. In contrast to purely statistical analyses of Compton- y maps—such as power spectra, stacking measurements, or cluster number counts—constrained simulations retain the spatial phase information of the density field, enabling object-by-object comparison between observed and simulated clusters and their environments. This allows explicit modelling of projection effects along the line of sight, identification of dominant contributors to the tSZ signal in specific directions, and physically motivated interpretation of residuals that would otherwise be absorbed into effective scatter or nuisance parameters. The simulations also provide a means of calibrating the mass–Compton- y relation that does not require any other mass proxy. Such considerations are particularly relevant in the local Universe, where a small number of massive clusters and supercluster environments dominate the tSZ signal.

We use digital twins, constrained simulations that sample the Bayesian posterior of the local density field, to investigate how tSZ observations can be interpreted and augmented by knowledge of the underlying large-scale structure. Building on BORG-based reconstructions, we construct digital twins of the nearby Universe that reproduce the observed positions of galaxy clusters with high fidelity, and compare their predicted thermal pressure distribution to observed Compton- y maps. Our analysis focuses on cluster matching, positional accuracy, and the correspondence between simulated and observed tSZ signals, rather than on deriving new cosmological constraints. By doing so, we demonstrate how digital twins provide a practical framework for extracting additional physical information from tSZ data and for validating assumptions underlying standard tSZ analyses,

while remaining complementary to established statistical approaches.

The paper is structured as follows. Section 2 describes the simulation suites and Compton- y maps employed, as well as the X-ray and optical cluster data used for further validation. Section 3 describes our methodology, including our approach for associating haloes between realisations in each suite and with Compton- y hotspots, the metric we develop for scoring the simulations on the basis of the Compton- y signal, and our method for fitting mass–mass and mass–observable scaling relations. Section 4 details the results, while Section 5 provides a literature comparison, situates our validation metric within a broader context and proposes future directions. Section 6 concludes.

2. DATA

We describe the constrained simulation suites used in this work (Section 2.1), the *Planck* tSZ map and cluster catalogue (Sections 2.2 and 2.3), the eROSITA X-ray cluster catalogue (Section 2.4), and the selection of nearby clusters for detailed analysis (Section 2.5).

2.1. Digital twins

We employ two suites of digital twins¹—CSiBORG2 (CB2) and CSiBORG-Manticore (CBM), the latter a new suite of digital twins introduced in this work—representing successive generations of reconstructions based on the BORG algorithm applied to the 2M++ galaxy catalogue (Lavaux and Hudson 2011). BORG produces a posterior distribution of voxel densities at $z = 1000$ by forward-modelling the initial conditions with redshift-space distortions, selection effects and galaxy biasing, and comparing to the observed galaxy number density via a Poisson likelihood (Jasche and Wandelt 2013; Jasche *et al.* 2015; Lavaux and Jasche 2016; Leclercq *et al.* 2017; Jasche and Lavaux 2019; Lavaux *et al.* 2019; Porqueres *et al.* 2019; Stopyra *et al.* 2024; McAlpine 2025). Each suite comprises multiple N -body simulations, each representing a single draw from the BORG posterior, thereby capturing uncertainties in the large-scale structure constraints while delivering high-resolution dark-matter simulations by adding random-phase small-scale modes consistent with the imposed large-scale density field and the Λ CDM power spectrum.

In both suites, constraints are imposed within the 2M++ region, a spherical volume of radius $\sim 155 h^{-1}$ Mpc centred on the Milky Way ($z \lesssim 0.05$), embedded in a periodic box of side length 1000 Mpc. Beyond this volume, the density field is largely unconstrained, serving only to provide the correct large-scale forces expected in Λ CDM. The BORG density field is sampled on a 256^3 grid with a resolution of 3.9 Mpc. We now briefly describe each suite in turn.

CB2 is the second iteration of the *Constrained Simulations in BORG* (CSiBORG) suite. It adopts a similar setup to the original CSiBORG (Bartlett *et al.* 2021) but uses the updated BORG initial conditions of Stopyra *et al.*

¹ While coming under the umbrella heading of “constrained simulations”, these are more precisely described as data-constrained posterior simulations, reflecting that their initial conditions are inferred via a full Bayesian forward model with explicit uncertainty quantification.

(2024). It comprises 20 dark matter-only N -body runs within a $677.7 h^{-1}$ Mpc box centred on the Milky Way. The BORG initial conditions employ a 20-step COLA integrator (Tassev *et al.* 2013) for improved accuracy, are linearly extrapolated to $z = 69$ and supplemented with small-scale white noise on a 2048^3 mesh covering the constrained 2M++ volume. This high-resolution zoom-in region, spanning the $\sim 155 h^{-1}$ Mpc radius where the 2M++ catalogue has highest completeness, yields a spatial resolution of $0.33 h^{-1}$ Mpc and a particle mass of $3 \times 10^9 h^{-1} M_\odot$. A $10 h^{-1}$ Mpc buffer zone surrounds this high-resolution region to ensure a smooth transition to the coarser outer volume, preventing artificial discontinuities in the density field at the boundary. The simulations are evolved to $z = 0$ using Gadget4 (Springel *et al.* 2021), adopting cosmological parameters from Planck Collaboration *et al.* (2020a) incorporating lensing and baryon acoustic oscillation data: $\Omega_m = 0.3111$, $\sigma_8 = 0.8102$, $H_0 = 67.66 \text{ km s}^{-1} \text{ Mpc}^{-1}$, $n_s = 0.9665$, $\Omega_b = 0.049$. We use 20 posterior samples resimulated for Stiskalek *et al.* (2025).

The CBM suite uses the Manticore-Local initial conditions from McAlpine *et al.* (2025), representing the most recent BORG reconstruction, resimulated with the CSiBORG zoom-in setup. We use 50 posterior samples, drawn from four independent chains, resimulated with Gadget4 using the same zoom-in parameters as CB2, yielding a particle mass of $3 \times 10^9 h^{-1} M_\odot$. The cosmological parameters are drawn from the Dark Energy Survey Year 3 “ 3×2 pt + All Ext.” Λ CDM analysis (Abbott *et al.* 2022): $h = 0.681$, $\Omega_m = 0.306$, $\Omega_\Lambda = 0.694$, $\Omega_b = 0.0486$, $A_s = 2.099 \times 10^{-9}$, $n_s = 0.967$, and $\sigma_8 = 0.807$. McAlpine *et al.* (2025) introduced these initial conditions along with the Manticore-Local suite, in which they are resimulated at a uniform 1024^3 resolution, and showed that it surpasses earlier reconstructions in velocity field tests, exhibits good agreement with observed cluster masses and positions, and produces a $z = 0$ power spectrum and halo mass function that are in excellent agreement with Λ CDM expectations. We adopt the CBM suite rather than Manticore-Local for convenience; while it offers higher particle resolution, this makes no significant difference for the massive haloes studied here.

2.2. Planck tSZ map

We use the *Planck* all-sky Compton- y map as our primary observational dataset for validating the tSZ signal in the constrained simulations. The amplitude of the tSZ effect is quantified by the Compton- y parameter, defined as

$$y \equiv \frac{\sigma_T}{m_e c^2} \int n_e(l) k_B T_e(l) dl, \quad (1)$$

where σ_T is the Thomson cross-section, m_e the electron mass, n_e and T_e are the electron number density and temperature, respectively, and the integral is taken along the line of sight l . The Compton- y parameter is therefore proportional to the integrated electron pressure,

$$P_e = n_e k_B T_e, \quad (2)$$

and directly traces the thermal energy content of ionised gas, with minimal sensitivity to gas clumping compared to X-ray observables. Observationally, the tSZ signal is

extracted from multi-frequency CMB data by exploiting its distinctive spectral dependence, which produces a decrement in CMB intensity below $\simeq 217$ GHz and an increment above it. Component-separation techniques applied to multi-band data from experiments such as *Planck*, ACT, or SPT are used to isolate the tSZ contribution and construct full-sky or partial-sky Compton- y maps (Collaboration 2016).

We use the all-sky Compton- y parameter map constructed from the *Planck* PR4 data release by McCarthy and Hill (2024). This map was produced using a Needlet Internal Linear Combination (NILC) pipeline applied to the nine *Planck* frequency channels from 30 to 857 GHz. The map employs a moment-based deprojection method to minimise contamination from the cosmic infrared background (CIB), which otherwise biases the recovered Compton- y signal at small angular scales. The map is consistent with the earlier *Planck* release (Planck Collaboration *et al.* 2016b) on large scales, but has 10–20% lower noise on small scales.

2.3. Planck tSZ cluster catalogue

We use the second *Planck* catalogue of Sunyaev-Zel'dovich sources (PSZ2; Planck Collaboration *et al.* 2016c)², which contains 1653 detections of which 1203 are confirmed clusters with identified counterparts; we restrict our analysis to the latter. The catalogue contains the integrated Compton- y parameter $Y_{5R_{500}}$ for each source, computed via aperture photometry within an angular radius corresponding to $5R_{500c}$. The cluster size R_{500c} is derived iteratively using a $Y_{500c} - \theta_{500c}$ prior combined with the $Y_{500c} - M_{500c}$ scaling relation from Planck Collaboration *et al.* (2014), itself calibrated to X-ray hydrostatic masses from the MCXC (Piffaretti *et al.* 2011).

We convert $Y_{5R_{500}}$ to Y_{500c}^{tSZ} using $Y_{5R_{500}} = 1.81 Y_{500c}^{\text{tSZ}}$, derived under the spherical assumption with the universal pressure profile (Arnaud *et al.* 2010; Planck Collaboration *et al.* 2011). We then convert to physical units by multiplying by $D_A^2(z)$, where $D_A(z)$ is the angular diameter distance computed from the observed heliocentric redshift. Finally, we apply the self-similar scaling by multiplying by $E(z)^{-2/3}$, where

$$E(z) = \sqrt{\Omega_m(1+z)^3 + 1 - \Omega_m}, \quad (3)$$

though this correction is negligible at $z < 0.05$. We use these measurements alongside the tSZ mass estimates reported in the catalogue to compare with predictions from the digital twin halo masses. Note that the reported masses are likely biased low by $\sim 30\%$ with respect to weak lensing masses (Sereno *et al.* 2017), and *Planck* cluster counts using tSZ masses yield a relatively low σ_8 compared to the fiducial *Planck* CMB analysis (Planck Collaboration *et al.* 2016a, 2020b). We therefore prefer to compare directly to Y_{500c}^{tSZ} rather than the derived masses, which may not be reliable, though we shall also show the mass comparison. We select clusters with $M_{500c}^{\text{tSZ}} > 10^{14} M_\odot$ and $z < 0.05$, yielding 56 clusters for our analysis.

² <https://heasarc.gsfc.nasa.gov/w3browse/all/plancksz2.html>

2.4. eROSITA X-ray cluster catalogue

We employ the eROSITA X-ray cluster catalogue primarily because its masses are calibrated via state-of-the-art weak gravitational lensing, providing an independent mass reference against which to compare the digital twin halo masses. We use the first eROSITA All-Sky Survey cluster catalogue (Bulbul *et al.* 2024), which contains 12,247 optically confirmed galaxy clusters and groups detected as extended X-ray sources in the western Galactic hemisphere. The catalogue covers $13,116 \text{ deg}^2$ observed during eROSITA’s first six months of operation aboard the Spectrum-Roentgen-Gamma satellite (Predehl *et al.* 2021). For each cluster, the catalogue reports X-ray properties including flux, luminosity $L_{500c}^{\text{X-ray}}$, and temperature, as well as derived quantities such as total mass $M_{500c}^{\text{X-ray}}$, and gas mass (see also Nguyen-Dang *et al.* 2024, for X-ray scaling relations from eFEDS).

Crucially, the eROSITA cluster masses are calibrated using weak gravitational lensing measurements from the Dark Energy Survey Year 3 data (Grandis *et al.* 2024). This calibration determines the scaling between X-ray count rate and halo mass by measuring the lensing signature in background galaxy shapes caused by eROSITA-selected clusters, using a Bayesian population model that accounts for sample selection, contamination and instrumental systematics. Applying the same selection criteria ($M_{500c}^{\text{X-ray}} > 10^{14} M_{\odot}$ and $z < 0.05$) yields 74 clusters in this case.

2.5. Selected nearby clusters

We select 18 well-known nearby clusters for detailed analysis, listed in Table 1. These clusters span a redshift range $0.005 \lesssim z \lesssim 0.050$ and are distributed across the sky, covering prominent superclusters including Hydra-Centaurus, Hercules, Coma, and Shapley. Clusters are labelled by their host supercluster where applicable, with their Abell catalogue designation (Abell 1958) in parentheses; multiple clusters sharing a supercluster name (e.g. Hercules) are distinct systems within the same optically identified large-scale overdensity, not necessarily gravitationally bound to one another. For each cluster, we report the observed Galactic coordinates (ℓ, b) and CMB-frame recession velocity cz_{CMB} obtained from NED³, along with masses from the *Planck* tSZ and eROSITA X-ray catalogues matched by angular separation and redshift. Where both masses are available, the weak-lensing-calibrated eROSITA masses are systematically higher than the tSZ masses, reflecting a known bias in the *Planck* tSZ mass calibration.

3. METHODOLOGY

We describe our methodology for comparing observed tSZ signals with predictions from constrained simulations. In Section 3.1, we detail how we measure the tSZ signal at halo positions, which is used for our named-cluster catalogue. In Section 3.2, we describe stacked radial profiles, which are used to test the mass dependence of the signal. In Section 3.3, we introduce halo associations, which link the same halo across realisations. In Sections 3.4 and 3.5, we describe the matching procedures used to link catalogues of observed clusters to

these associations. Finally, in Section 3.6, we describe the Bayesian linear regression used to fit scaling relations while marginalising over the mass uncertainty.

3.1. tSZ signal at halo positions

We measure the tSZ signal of each halo using aperture photometry on a Compton- y map in HEALPix⁴ format (Górski *et al.* 2005). For a given pointing and aperture radius θ_{ap} , we use the `healpy`⁵ implementation (Zonca *et al.* 2019) to identify all HEALPix pixels within the circular aperture. We apply a mask to exclude invalid regions, including the Galactic plane, point sources, and pixels marked as unseen. The enclosed signal is then computed as the arithmetic mean of the Compton- y values over all valid pixels within the aperture. For each halo, we set the aperture radius equal to $2\theta_{500c}$, where θ_{500c} is the angular radius corresponding to R_{500c} at the halo’s comoving distance and R_{500c} is the radius within which the mean density is 500 times the critical density.

To assess the significance of the measured signal, we compute an empirical p_{tSZ} -value by comparing it to a null distribution obtained from random sky positions. We measure the enclosed signal at $N_{\text{rand}} = 10^5$ random pointings, excluding the Galactic plane, at the same aperture size as the halo. The halo’s signal S is then ranked within this distribution, and the p_{tSZ} -value is

$$p_{\text{tSZ}} = 1 - \frac{\text{rank}(S)}{N_{\text{rand}}}. \quad (4)$$

This p_{tSZ} represents the fraction of random pointings with a signal equal to or exceeding S , i.e. the probability of observing a signal as high as S by chance. A low p_{tSZ} therefore indicates that the measured signal is significantly higher than expected from random sky positions. p_{tSZ} is sensitive to the halo’s angular position on the sky, as different regions exhibit varying noise and foreground contamination levels, and partly to its physical size via the aperture radius.

3.2. Stacked 1D radial profiles

To construct average radial profiles across multiple sources, we stack individual profiles measured at normalised radii. For each source with angular size θ_{500c} , we measure the enclosed signal at normalised angular separations $\theta/(2\theta_{500c})$, yielding a radial profile that can be compared across sources of different angular sizes arising from their varying distances and masses. The stacked profile is then computed as the mean across all sources at each normalised radius, with uncertainties estimated via bootstrap resampling. To assess the significance of the stacked signal, we construct random stacks by measuring profiles at random sky positions, with aperture sizes resampled from the distribution of source angular sizes. Each random stack contains the same number of profiles as the data stack, and we repeat this process many times to build a null distribution.

⁴ <https://healpix.sourceforge.io>

⁵ <https://healpy.readthedocs.io/en/latest/>

TABLE 1

SELECTED NEARBY CLUSTERS FOR DETAILED ANALYSIS, ORDERED BY RECESSION VELOCITY. WE REPORT THE GALACTIC LONGITUDE ℓ , GALACTIC LATITUDE b , CMB-FRAME RECESSION VELOCITY cz_{CMB} , THE *Planck* TSZ MASS (PLANCK COLLABORATION *et al.* 2016c), AND THE WEAK-LENSING-CALIBRATED EROSITA MASS (BULBUL *et al.* 2024), WHERE AVAILABLE. VIRGO LACKS A TSZ MASS DUE TO ITS LARGE ANGULAR EXTENT RELATIVE TO THE *Planck* BEAM; OTHER CLUSTERS MAY BE ABSENT DUE TO PROXIMITY TO THE ZONE OF AVOIDANCE. SOME CLUSTERS LACK EROSITA MASSES DUE TO THE HALF-SKY COVERAGE OF THE eRASS1 DATA RELEASE.

Cluster	cz_{CMB} [km s $^{-1}$]	ℓ [deg]	b [deg]	$\log M_{500c}^{\text{TSZ}}$ [M_{\odot}]	$\log M_{500c}^{\text{X-ray}}$ [M_{\odot}]
Virgo	1636	283.8	74.4	—	—
Centaurus (A3526)	3403	302.4	21.6	14.12	14.43
Hydra (A1060)	4058	269.6	26.5	—	14.20
Norma (A3627)	4955	325.3	-7.1	14.38	14.61
Perseus (A426)	4995	150.6	-13.3	—	—
Leo (A1367)	6890	235.1	73.0	14.22	14.55
Coma (A1656)	7463	58.1	88.0	14.86	—
Hercules (A2199)	9113	62.9	43.7	14.46	—
Abell 496	9849	209.6	-36.5	14.43	14.83
Hercules (A2063)	10634	12.9	49.7	14.28	—
Hercules (A2151)	11024	31.6	44.5	—	—
Hercules (A2147)	11072	29.0	44.5	14.55	—
Shapley (A3571)	11965	316.3	28.6	14.67	14.82
Abell 548	12363	230.3	-24.8	—	13.68
Abell 119	13004	125.7	-64.1	14.54	—
Abell 1736	13823	312.6	35.0	14.46	—
Abell 1644	14448	304.9	45.5	14.57	14.59
Shapley (A3558)	14784	312.0	30.7	14.68	14.81

3.3. Halo associations

Halo associations were introduced by McAlpine (2025) to identify the “same” halo across realisations of the BORG posterior represented by the suite of digital twins. An association is a set of haloes (at most one per realisation) that reside at approximately the same position at $z = 0$ and have similar masses. Following McAlpine (2025), we identify associations using the DBSCAN clustering algorithm with linking length $\epsilon = 1.75 h^{-1}$ Mpc and a minimum membership of nine. When multiple haloes from the same realisation fall into the same cluster, we retain only the one closest to the centroid (the mean position of all cluster members), since associations are defined to contain at most one halo per realisation. We additionally discard any outliers whose masses deviate by more than 0.3 dex from the mean logarithmic mass of the association members, and recalculate the centroid from the surviving members. Each association is furthermore characterised by f_{present} , defined as the number of member haloes divided by the total number of realisations.

3.4. Classical matching

We match observed clusters from the *Planck* tSZ catalogue to halo associations using a classical angular separation and redshift criterion. For each observed cluster-association pair, we compute the angular separation on the sky and the line-of-sight velocity difference $\Delta cz = |cz_{\text{obs}} - cz_{\text{sim}}|$ in the CMB frame, where cz_{obs} and cz_{sim} are the recessional velocities of the observed cluster and simulated halo, respectively. The redshift of the simulated halo is computed as

$$1 + z_{\text{sim}} = (1 + z_{\text{cosmo}})(1 + z_{\text{pec}}), \quad (5)$$

where z_{cosmo} is the cosmological redshift corresponding to the halo’s comoving distance and $z_{\text{pec}} = V_{\text{los}}/c$ is the Doppler shift from its peculiar velocity V_{los} along the line of sight. A pair is considered a valid candidate if $\Delta\theta < 60'$ and $\Delta cz < 300 \text{ km s}^{-1}$. We further require that at least 50% of the association’s member haloes satisfy

both criteria, ensuring robust matches even for associations with significant positional scatter. We opt for relatively stringent matching criteria to minimise spurious matches, which would tend to flatten the inferred scaling relation slopes; we note that additional halo–cluster pairs lie just beyond these thresholds and would likely constitute valid matches.

Among the valid candidate pairs, we assign matches using a greedy algorithm that minimises the three-dimensional redshift-space comoving distance between the observed cluster position and the association centroid. At each iteration, the algorithm selects the pair with the smallest distance, assigns the match, and removes both the cluster and association from further consideration. This process continues until no valid pairs remain.

3.5. LUM matching

For our set of 18 named nearby clusters (described in Section 2), we employ the Local Universe Model (LUM) matching procedure based on Pfeifer *et al.* (2023) that quantifies the significance of each cluster-halo association. We note that the classical matching procedure would yield very similar pairs; however, the LUM approach provides additional insight into the match significance. For a halo of mass M_{200c} at distance r from the observed cluster position, we compute the cumulative probability of finding such a halo within that distance under the assumption of a uniform spatial distribution. Here M_{200c} is the mass enclosed within R_{200c} , the radius within which the mean density is 200 times the critical density of the Universe. The probability density of finding the nearest halo at distance r is

$$p(r) = 4\pi r^2 n(M_{200c}) \exp\left[-\frac{4}{3}\pi r^3 n(M_{200c})\right], \quad (6)$$

where $n(M_{200c})$ is the halo mass function evaluated at $z = 0$ using the `colossus` package (Diemer 2018) with the model of Tinker *et al.* (2008). The cumulative distri-

bution function, representing the probability of finding a halo within distance r , is

$$p_{\text{LUM}} = 1 - \exp \left[-\frac{4}{3} \pi r^3 n(M_{200c}) \right]. \quad (7)$$

A low value of p_{LUM} indicates that the halo is closer than expected by chance, suggesting a significant match; p_{LUM} can thus be interpreted as a p -value under the null hypothesis that the halo–cluster proximity arose by chance. Note that p_{LUM} depends on both the halo mass and distance: more massive haloes are rarer and thus a match at a given distance is more significant. For each observed cluster, we compute p_{LUM} for all haloes within a maximum search radius and select the match with the lowest value, subject to a threshold on the maximum allowed p_{LUM} . Since each association contains multiple haloes from different realisations, we compute p_{LUM} for each member halo, yielding a distribution of p_{LUM} -values that characterises the match quality across the ensemble. To summarise the match quality for a cluster-association pair, we take the median p_{LUM} across all member haloes.

To assign matches, we first compute the median p_{LUM} over member haloes for each observed cluster-association pair, forming a matrix. We then apply a greedy algorithm: at each iteration, we select the pair with the lowest median p_{LUM} , assign the match, and remove both the cluster and association from further consideration. The process continues until no pairs remain below a specified threshold.

3.6. Scaling relation fitting

To fit scaling relations between catalogue quantities (e.g., $\log Y_{500c}^{\text{tSZ}}$ or calibrated mass) and **BORG** halo masses, we use a linear regression model that accounts for the uncertainty in the simulated masses, which are the independent variable. For each matched association, we have a distribution of halo masses from the member haloes across realisations, rather than an estimate with Gaussian uncertainty. We fit a linear model

$$y = m \log \left(\frac{M_{500c}^{\text{BORG}}}{10^{14} h^{-1} M_{\odot}} \right) + c, \quad (8)$$

where y is the logarithm of the catalogue quantity with Gaussian error σ_y , M_{500c}^{BORG} is the halo mass from **BORG** (the mass enclosed within R_{500c}), m is the slope, and c is the intercept. We similarly normalise the dependent variable: for catalogue masses we use $y = \log(M_{500c}/(10^{14} h^{-1} M_{\odot}))$, for X-ray luminosities $y = \log(L_{500}/(10^{44} \text{ erg s}^{-1}))$, and for the integrated Compton- y parameter $y = \log(Y_{500c}^{\text{tSZ}}/(10^{-4} \text{ Mpc}^2))$. Pivoting the variables near their mean values reduces covariance between m and c . We also include an intrinsic scatter σ_{int} as a free parameter, which is added in quadrature to the observational error.

To account for the mass uncertainty, we marginalise over the mass samples. Assuming that the matched clusters are independent, the total likelihood is the product of individual likelihoods. For each observed cluster i with mass samples $\{M_i^{(k)}\}_{k=1}^K$ from its matched association,

the likelihood is

$$\mathcal{L}_i = \frac{1}{K} \sum_{k=1}^K \mathcal{N} \left(y_i \mid m \log \frac{M_i^{(k)}}{10^{14} h^{-1} M_{\odot}} + c, \sqrt{\sigma_{y,i}^2 + \sigma_{\text{int}}^2} \right), \quad (9)$$

where $\mathcal{N}(y \mid \mu, \sigma)$ is a probability density function of a Gaussian distribution with mean μ and standard deviation σ . We adopt flat priors on m , c , and σ_{int} . To sample the posterior distribution we use the No-U-Turn Sampler (NUTS; Hoffman and Gelman 2011) method of Hamiltonian Monte Carlo (HMC) as implemented in the `numpyro`⁶ package (Phan et al. 2019; Bingham et al. 2019), collecting approximately 10^4 effective samples and ensuring a Gelman–Rubin statistic $\hat{R} - 1 \leq 0.001$ for convergence (Gelman and Rubin 1992).

To quantify the monotonic correlation between predicted and observed quantities, we compute the Spearman rank correlation coefficient ρ_s . We estimate its uncertainty by resampling: in each of 10^4 iterations, we draw x and y from Gaussian distributions centred on their measured values with standard deviations equal to their uncertainties, and compute ρ_s for the resampled data. We report the median and standard deviation of the resulting distribution.

We then calculate a significance τ at which the fitted scaling relation is in tension with theoretical expectations. Under the self-similar model of cluster formation and hydrostatic equilibrium, the integrated Compton- y signal within a characteristic radius (often R_{500}) scales with halo mass as $Y \propto M^m E^{2/3}(z)$, where $E(z) \equiv H(z)/H_0$ and $m \sim 5/3$. For soft-band X-ray luminosity, the self-similar expectation is $L_X \propto M^{4/3}$, applicable to eROSITA’s 0.5–2 keV band. This assumes purely gravitational cluster formation, hydrostatic and virial equilibrium, constant gas fraction and the non-relativistic limit (Kaiser 1986; Arnaud et al. 2010). We therefore compute the marginal tension for the observable–mass relations as $\tau_m = |\bar{m} - m_{\text{ss}}|/\sigma_m$, where \bar{m} is the posterior mean, σ_m is the posterior standard deviation of the slope, and m_{ss} is the self-similar expectation (5/3 for tSZ, 4/3 for X-ray). For mass–mass relations, where the expectation is a one-to-one correspondence ($m = 1$, $c = 0$)—the latter following from pivoting both variables at the same value—we compute a joint tension using the Mahalanobis distance: $d^2 = (\boldsymbol{\theta} - \boldsymbol{\mu})^T \boldsymbol{\Sigma}^{-1} (\boldsymbol{\theta} - \boldsymbol{\mu})$, where $\boldsymbol{\theta} = (1, 0)^T$ is the target, $\boldsymbol{\mu}$ is the posterior mean of (m, c) , and $\boldsymbol{\Sigma}$ is the posterior covariance matrix. We convert d^2 to a p -value via the χ^2 distribution with two degrees of freedom, $p = 1 - F_{\chi^2}(d^2; 2)$, and then to an equivalent Gaussian significance $\tau_{m,c} = \Phi^{-1}(1 - p/2)$, where Φ^{-1} is the inverse standard normal cumulative distribution function.

4. RESULTS

We present our validation of constrained simulations against tSZ observations in three parts: per-cluster angular positioning tests (Section 4.1), stacked radial profiles as a function of halo mass (Section 4.2), and mass scaling relations for matched cluster samples (Section 4.3).

⁶ <https://num.pyro.ai/en/latest/>

4.1. Scoring angular position

We assess the angular positioning of simulated haloes by computing the tSZ signal at each observed cluster position and comparing it against random sky locations to derive a p -value, p_{tSZ} , for each cluster in each realisation. For the majority of clusters, we find $p_{\text{tSZ}} < 0.05$ across all realisations, indicating that the simulations place haloes at the correct angular positions (Fig. 1). The results are broadly consistent between CB2 and CBM, with both simulations yielding significant detections for most selected clusters. Coma and Shapley (A3558) are among the best-reproduced clusters in both simulations, with $\tilde{p}_{\text{tSZ}} < 10^{-3}$.

A notable exception is Perseus, for which we find no counterpart in CB2 but which is among the best-reproduced clusters in CBM ($\tilde{p}_{\text{tSZ}} = 2.9 \times 10^{-4}$). Perseus is the archetypal cool-core cluster, with a sharply peaked X-ray surface brightness, short central cooling time, and active active galactic nucleus (AGN) feedback from NGC 1275 (Fabian *et al.* 2006). The compact, centrally concentrated tSZ signal characteristic of cool cores is evident in Fig. 2. Conversely, Hercules (A2151) is poorly reproduced in CBM ($\tilde{p}_{\text{tSZ}} = 0.45$, $f_{\text{present}} = 0.54$) while no counterpart is found in CB2. Norma is well reproduced in both simulations ($p_{\text{LUM}} = 2.1 \times 10^{-2}$ in CB2 and 8.7×10^{-5} in CBM); however, its low Galactic latitude ($b \approx -7^\circ$) places it within the masked region of the Compton- y map, precluding a p_{tSZ} assessment. We note that CBM yields systematically higher halo masses than CB2 for the matched clusters (Table 3); we defer discussion of these mass differences to Section 4.3.

Fig. 2 shows tSZ map cutouts for selected clusters, illustrating the angular correspondence between the CBM haloes and the observed signal. We exclude Norma (masked), Virgo (nearby with extended tSZ signature), and Shapley (A3562), Hercules (A2151 and A2063), Abell 1644, and Abell 548 (all with relatively high \tilde{p}_{tSZ} values) from this visualisation (Table 3).

In both Shapley and Hercules, the CBM halo positions exhibit systematic offsets towards neighbouring clusters, possibly indicating that BORG merges clusters along filamentary structures into a single halo. Within Shapley, halo positions are offset from the tSZ and optical centres of A3558 towards A3562. Dynamical mass estimates from Haines *et al.* (2018) yield $M_{\text{dyn}} = (14.8 \pm 1.4) \times 10^{14} M_{\odot}$ for A3558 and $(6.6 \pm 0.8) \times 10^{14} M_{\odot}$ for A3562, while weak lensing measurements by Higuchi *et al.* (2020) give $M_{200c} = 4.5_{-2.4}^{+2.8} \times 10^{14} h^{-1} M_{\odot}$ and $2.0_{-1.8}^{+2.7} \times 10^{14} h^{-1} M_{\odot}$, respectively. A3558 is a dynamically disturbed post-merger system, with X-ray observations revealing cold fronts extending to ~ 1.2 Mpc (Rossetti *et al.* 2007; Mirakhor *et al.* 2023). The complex may itself be the remnant of a cluster-cluster collision within the Shapley core (Bardelli *et al.* 1998), implying that hydrostatic mass estimates are potentially biased. Within Hercules, halo positions are similarly oriented towards A2151; this is consistent with A2147 being the dominant mass concentration, as dynamical estimates from Monteiro-Oliveira *et al.* (2022) find A2147 ($M \approx 13.5 \times 10^{14} M_{\odot}$) to be nearly five times more massive than A2151 ($M \approx 2.9 \times 10^{14} M_{\odot}$).

For comparison, we apply the same p_{tSZ} procedure

to clusters from the SLOW constrained hydrodynamical simulation (Hernández-Martínez *et al.* 2024), using the simulated halo positions reported in their Table A.1. Of the clusters in our sample (Table 1), only Perseus ($p_{\text{tSZ}} = 0.008$) and Shapley (A3558; $p_{\text{tSZ}} = 0.04$) achieve $p_{\text{tSZ}} < 0.05$ in SLOW, though both still have large angular offsets from the observed clusters of 15.8° and 13.4° , respectively; Virgo has $p_{\text{tSZ}} = 0.09$ with an angular offset of 8.7° . Notably, Coma—one of the most massive clusters in the local Universe—has $p_{\text{tSZ}} = 0.87$ in SLOW, owing to the angular offset of $\sim 15^\circ$ between the simulated halo and the observed counterpart, far larger than the $\lesssim 1^\circ$ offsets typical of BORG-based reconstructions (Fig. 2). By contrast, the majority of clusters in CBM achieve $p_{\text{tSZ}} < 0.05$, with the exceptions of Centaurus, Hydra, and Hercules (A2063), which have $\tilde{p}_{\text{tSZ}} \approx 0.1$ – 0.3 , and Hercules (A2151) and Abell 548, which have $\tilde{p}_{\text{tSZ}} \approx 0.4$.

4.2. Scoring stacked profiles

Rather than focusing on individual well-known systems, we now assess the mass dependence of the tSZ signal by stacking one-dimensional radial profiles as a function of halo mass. Following Section 3.2, we measure 1D radial profiles at normalised angular separations $\theta/(2\theta_{500c})$, where θ_{500c} is the angular radius corresponding to R_{500c} , for haloes in each realisation and stack them in mass-ranked bins to capture the expected trend of increasing signal with mass. We do not adjust the angular positions of the haloes; we simply extract the Compton- y map within an aperture centred on each halo’s sky position. We define three cumulative bins: the top 10, top 50, and top 100 most massive haloes in each realisation, and then stack the resulting profiles across all realisations within each simulation. This binning choice is designed to reveal the mass dependence while accounting for the systematic offset in halo masses between CB2 and CBM (Table 3); ranking by mass within each realisation ensures a fair comparison despite this offset.

Fig. 3 shows the stacked profiles for each bin, compared to random stacks constructed from uniformly distributed sky positions with aperture sizes drawn from the same distribution as the data.

For the top-10 and top-50 bins, both simulations yield a clear signal that is elevated above the random expectation across all radii. In the top-10 bin, CBM produces a marginally stronger signal than CB2. The top-50 bin shows a similar trend, with both simulations remaining well separated from the random baseline. In the top-100 bin, the signal weakens and approaches the random expectation, primarily reflecting the fact that lower-mass haloes are not as well angularly aligned with their true counterparts.

4.3. Scoring mass agreement

We now return to halo associations and match observed clusters using the classical matching procedure described in Section 3.4, requiring $\Delta\theta < 60'$ and $\Delta cz < 300 \text{ km s}^{-1}$. The matched fractions are similar across simulations: for eROSITA (Bulbul *et al.* 2024), we match 21/74 clusters in CB2 and 23/74 in CBM; for Planck, 13/56 in CB2 and 15/56 in CBM. For visualisation, we show the fraction of matched clusters as a function of the catalogue-

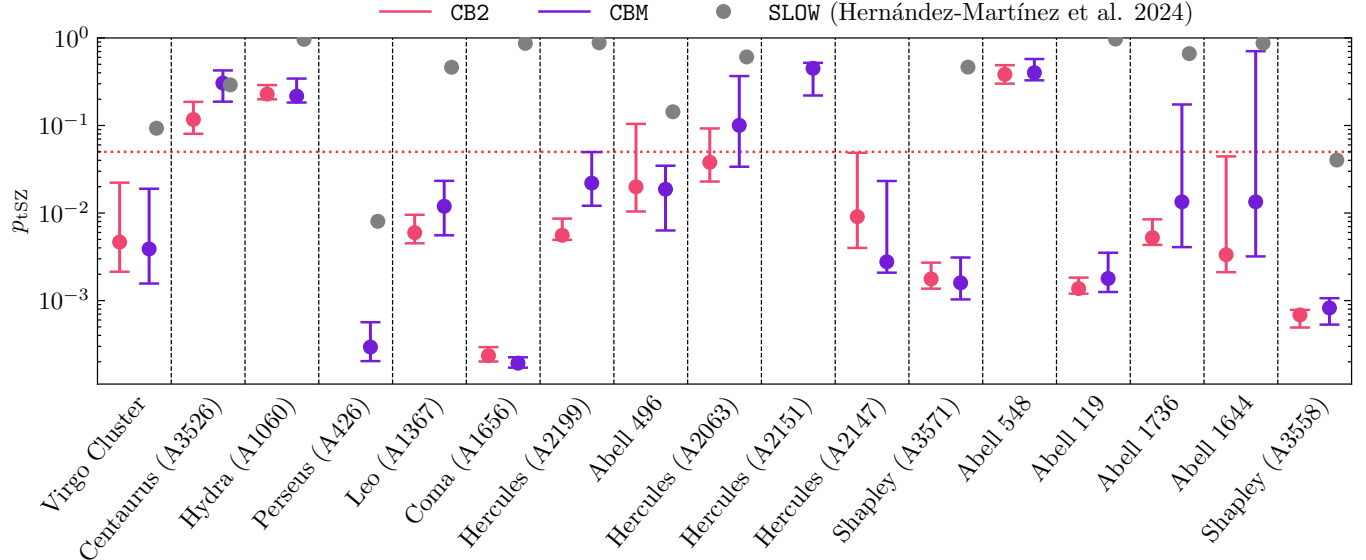


FIG. 1.— Distribution of p_{tSZ} for selected clusters from Table 1 across realisations in CB2 and CBM. For each cluster, p_{tSZ} is the fraction of random sky positions that yield an equal or higher tSZ signal than the observed cluster position; low values indicate that the simulated halo lies at the observed tSZ hotspot, indicative of a well-reconstructed cluster. The horizontal dashed line marks $p_{\text{tSZ}} = 0.05$. We also show p_{tSZ} values for SLOW clusters (Hernández-Martínez et al. 2024), computed using the same procedure with their simulated halo positions.

reported mass in Fig. 8 (Appendix), dividing the catalogues into percentile bins above $M_{500c} = 10^{14} M_{\odot}$; in the highest-mass bin, approximately half of the clusters are matched in both eROSITA and *Planck* for both simulations. These fractions would increase with looser matching criteria, but we opt for stringent thresholds to minimise spurious matches that would flatten the inferred scaling relation slopes. This makes our results conservative.

We exclude Shapley (A3558) from the mass scaling analysis due to a significant mass discrepancy: the CBM halo has $\log(M_{500c}/M_{\odot}) = 15.24 \pm 0.12$, compared to 14.68 ± 0.02 from *Planck* tSZ and 14.81 ± 0.04 from eROSITA. This may arise because A3558 lies near the edge of 2M++ completeness, where reconstruction fidelity is lower, or because BORG lacks the resolution to separate neighbouring structures along the Shapley filament, instead merging them into a single massive halo. The cluster itself is dynamically complex: dynamical mass estimates from Haines et al. (2018) yield $M_{\text{dyn}} = (14.8 \pm 1.4) \times 10^{14} M_{\odot}$, whereas the weak-lensing mass from Higuchi et al. (2020) is $\log(M_{200c}/h^{-1} M_{\odot}) = 14.65^{+0.21}_{-0.33}$ —a factor of ~ 2 lower. X-ray observations reveal large-scale sloshing and cold fronts extending to ~ 1.2 Mpc (Rossetti et al. 2007; Mirakhor et al. 2023), consistent with A3558 being a post-merger system, possibly from a collision within the Shapley core (Bardelli et al. 1998).

4.3.1. tSZ-mass scaling

The integrated Compton parameter Y_{500c}^{tSZ} scales with cluster mass as $Y_{500c}^{\text{tSZ}} \propto M_{500c}^m$, where self-similar theory predicts $m = 5/3$ (Kaiser 1986). Observationally, the $Y_{500c}^{\text{tSZ}}-M$ relation is found to be remarkably close to this prediction, with slopes $m \approx 1.7-1.8$ (Arnaud et al. 2010; *Planck* Collaboration et al. 2014). For the matched *Planck* clusters, we find slopes of $m = 1.43 \pm 0.31$ for CB2 and $m = 1.79 \pm 0.28$ for CBM (Table 2, Appendix),

both consistent with the self-similar expectation within uncertainties, though CBM yields a slope closer to the expected value. The Spearman correlation coefficients are high for both simulations ($\rho_s = 0.74 \pm 0.11$), indicating a strong monotonic relationship between the BORG halo masses and the observed Y_{500c}^{tSZ} . CBM yields a notably lower intrinsic scatter ($\sigma_{\text{int}} = 0.09 \pm 0.07$ dex) than CB2 ($\sigma_{\text{int}} = 0.23 \pm 0.09$ dex).

4.3.2. tSZ and X-ray derived mass scaling

We now examine the overall normalisation of the halo masses by comparing the *Planck*-calibrated masses M_{500c}^{tSZ} directly to the BORG halo masses, where the expectation is a one-to-one relation ($m = 1, c = 0$). For CBM, we find a slope of $m = 1.12 \pm 0.17$, consistent with unity, whereas CB2 yields a shallower slope of $m = 0.76 \pm 0.18$. The Spearman correlations are high for both simulations ($\rho_s = 0.79 \pm 0.09$ for CBM and $\rho_s = 0.74 \pm 0.09$ for CB2), indicating a strong monotonic relationship. The intercepts indicate a systematic offset in mass normalisation: CBM has $c = -0.20 \pm 0.07$, indicating that the BORG halo masses are systematically larger than the tSZ-calibrated masses by ~ 0.2 dex (a factor of ~ 1.6), with a joint tension of 4.7σ from the one-to-one relation. For CB2, the offset is weaker ($c = -0.02 \pm 0.07$, 2.2σ tension), though even here the majority of matched clusters have BORG masses exceeding the tSZ calibration. However, these offsets are consistent with the known $\sim 30\%$ bias of *Planck* tSZ masses relative to weak lensing calibrations (Sereno et al. 2017), suggesting that the BORG halo masses may more accurately reflect the true cluster masses.

We verify this bias by directly comparing the *Planck* tSZ masses to the weak-lensing-calibrated eROSITA X-ray masses for clusters matched between the two catalogues using $\Delta\theta < 15'$ and $\Delta cz < 300 \text{ km s}^{-1}$ (Fig. 4). We fit a linear relation in log-space using the roxy⁷

⁷ <https://github.com/DeaglanBartlett/roxy>

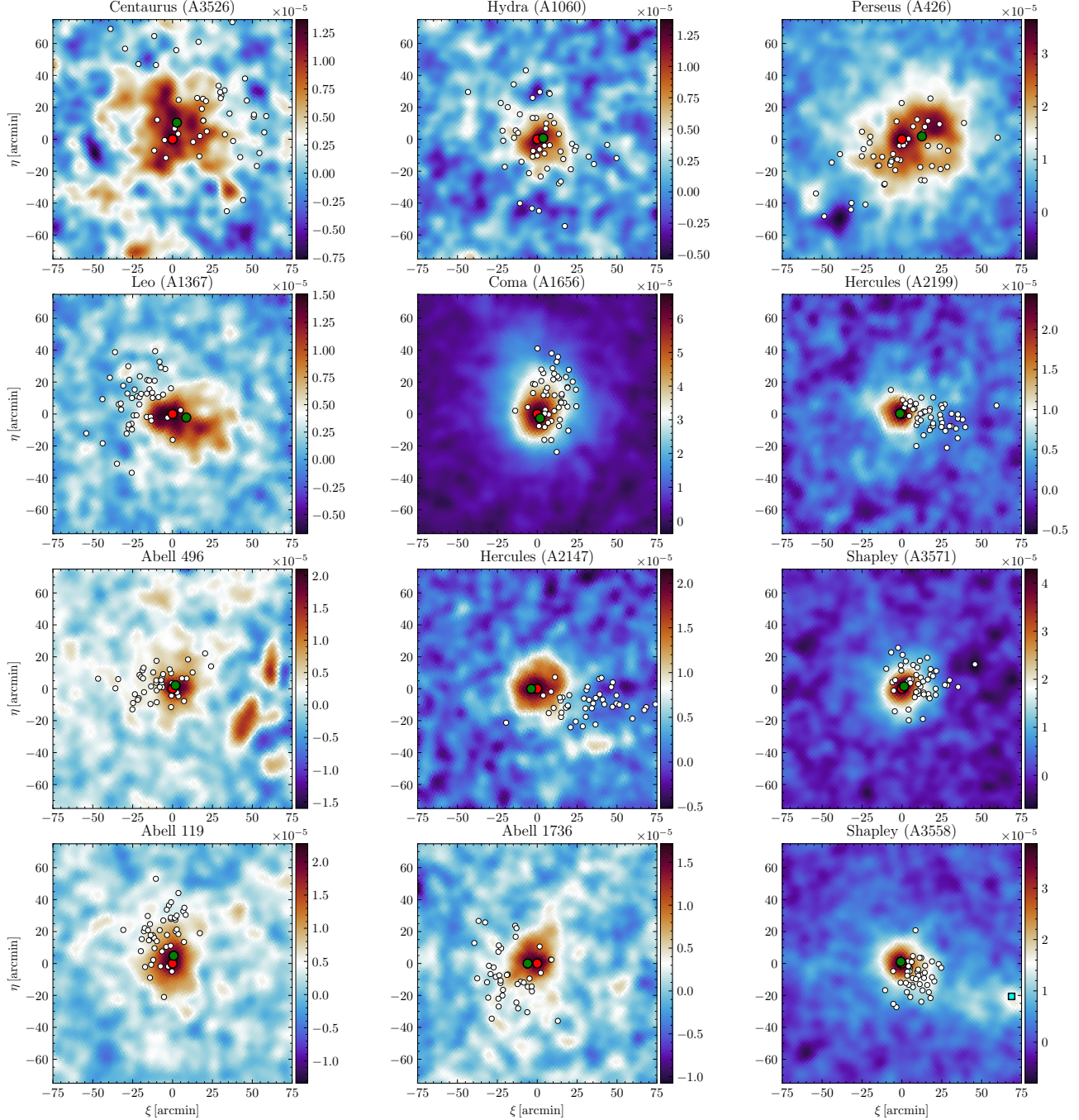


FIG. 2.— Compton- y map cutouts centred on selected clusters. White dots mark the positions of CBM halo realisations, the green dot indicates the reported cluster centre from the optical catalogue, and the red dot marks the local peak of the tSZ map. For Shapley (A3558), the cyan dot marks the position of Shapley (A3562), which lies within the field of view.

package (Bartlett and Desmond 2023), which implements Marginalised Normal Regression (MNR) to account for measurement uncertainties in both variables by placing a Gaussian hyperprior on the true value of the independent variable, pivoting both variables at $\log(M_{500c}/M_\odot) = 14$. We find a slope of $m = 1.01 \pm 0.04$, consistent with unity, and an intercept of $c = -0.14 \pm 0.03$, confirming that the *Planck* tSZ masses are systematically lower than the eROSITA X-ray masses by ~ 0.14 dex ($\sim 30\%$). Given this known bias in the tSZ mass calibration, it is not surprising that the CBM halo masses—which are derived from the underlying dark matter distribution—

exceed the *Planck*-reported values.

We perform an analogous comparison using the weak-lensing-calibrated eROSITA X-ray masses (Fig. 6). For CBM, we find a slope of $m = 0.84 \pm 0.19$ and an intercept of $c = 0.02 \pm 0.06$, in excellent agreement with the one-to-one relation (0.5σ tension), with a Spearman correlation of $\rho_s = 0.62 \pm 0.10$. In contrast, CB2 yields a shallower slope of $m = 0.75 \pm 0.21$ with a positive intercept $c = 0.12 \pm 0.05$, deviating from the expected relation at 2.1σ ; the correlation is also weaker ($\rho_s = 0.49 \pm 0.10$). This suggests that CBM halo masses are well calibrated against the weak-lensing-based eROSITA masses, whereas CB2

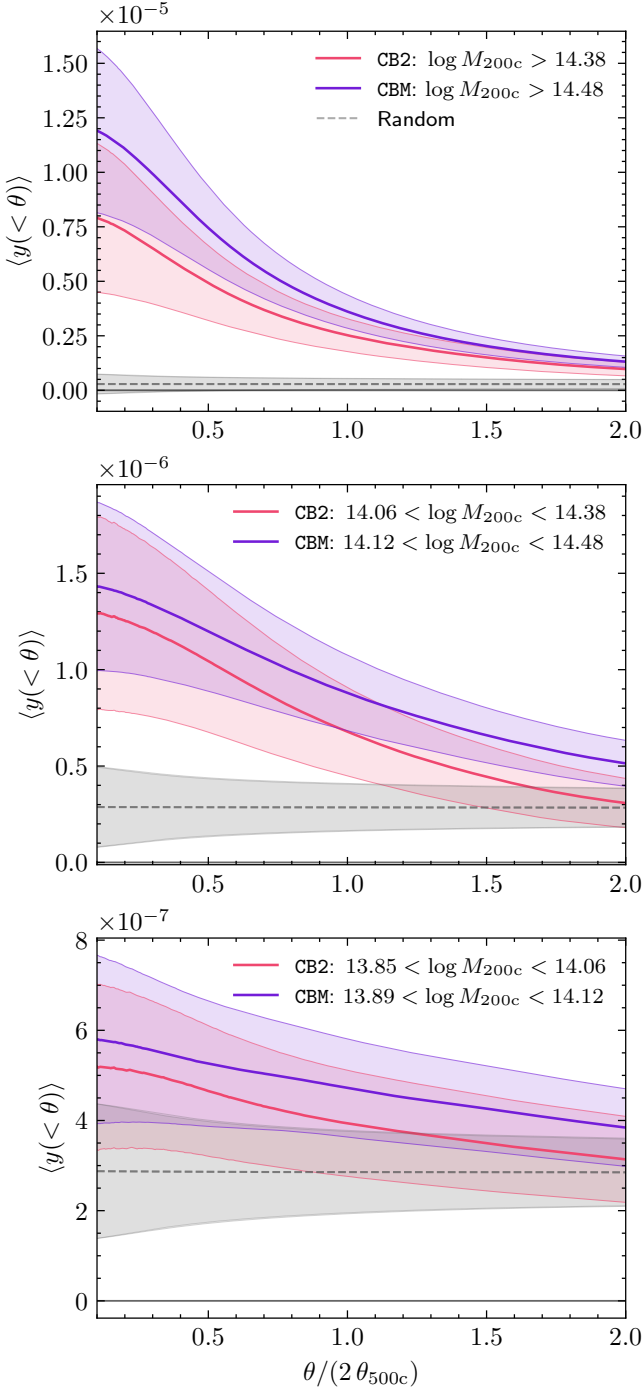


FIG. 3.— Stacked 1D radial tSZ profiles for haloes ranked by mass. Profiles are measured at normalised angular separations $\theta/(2\theta_{500c})$ and stacked within cumulative mass bins: top 10, top 50, and top 100 most massive haloes per realisation, then combined across all realisations. Halo masses M_{200c} are in units of $h^{-1} M_{\odot}$. Solid lines show the mean stacked profile for CB2 and CBM, with shaded bands indicating the 1σ uncertainty from bootstrap resampling. The grey band shows the random expectation from stacking at random sky positions. Both simulations show a clear signal above random in the top 10 and top 50 bins, with CBM marginally stronger in the top 10. The signal weakens in the top 100 bin, approaching the random baseline.

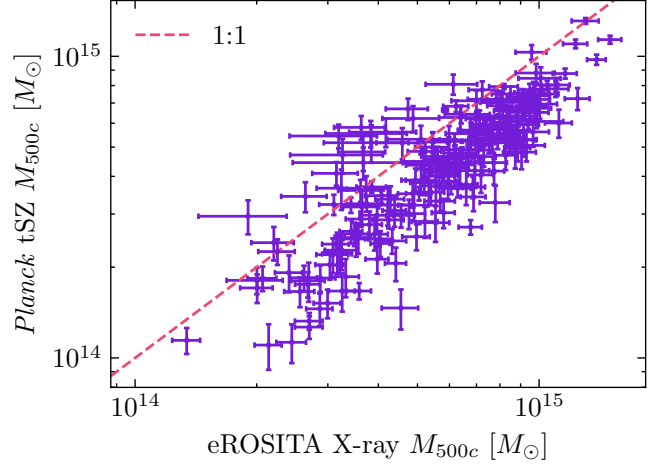


FIG. 4.— Comparison of Planck tSZ masses and eROSITA X-ray masses for matched clusters; error bars show 1σ uncertainties. The dashed line shows the one-to-one relation. The Planck masses are systematically lower by ~ 0.14 dex ($\sim 30\%$), consistent with the known hydrostatic mass bias (Sereno *et al.* 2017).

masses are systematically lower at the high-mass end.

5. DISCUSSION

Bayesian reconstructions of the local Universe have advanced from early smoothed density field estimates to full digital twins that reproduce the positions, masses, and velocities of individual structures (Jasche and Lavaux 2019; Stopyra *et al.* 2024; McAlpine *et al.* 2025). As these reconstructions achieve ever-higher fidelity, robust validation demands an expanding suite of independent tests; velocity field comparisons offer one such metric (Stiskalek *et al.* 2025), but a broader range of observables is needed. McAlpine *et al.* (2025) proposed a comprehensive validation framework for **Manticore-Local**, including posterior predictive tests of power spectra, bispectra, the initial white noise field, and the halo mass function, alongside cluster matching and peculiar velocity comparisons.

Among such tests, the tSZ effect offers a compelling probe: it traces the thermal energy of the intracluster medium, depends sensitively on halo mass through well-understood scaling relations, probes the angular positioning of clusters on the sky, and is measured with near-full-sky coverage by *Planck*. In this section, we first compare our results to other constrained simulation efforts (Section 5.1), then discuss the validation metrics employed in this work (Section 5.2), and finally discuss ways in which the work could be taken further (Section 5.3).

5.1. Comparison to literature

Beyond the **BORG** framework, constrained simulations of the local Universe have a long history of connecting observed large-scale structure to physically motivated predictions for cluster-scale observables. Early work used IRAS galaxy data to constrain initial conditions within $\sim 110 h^{-1}$ Mpc (Dolag *et al.* 2005), enabling detailed comparisons between simulated and observed nearby clusters such as Coma and Virgo. A particularly direct link to baryonic observables was established when the *Planck* collaboration combined tSZ and X-ray data with a constrained simulation of the Virgo environment to infer its distance and gas content (Planck Collabora-

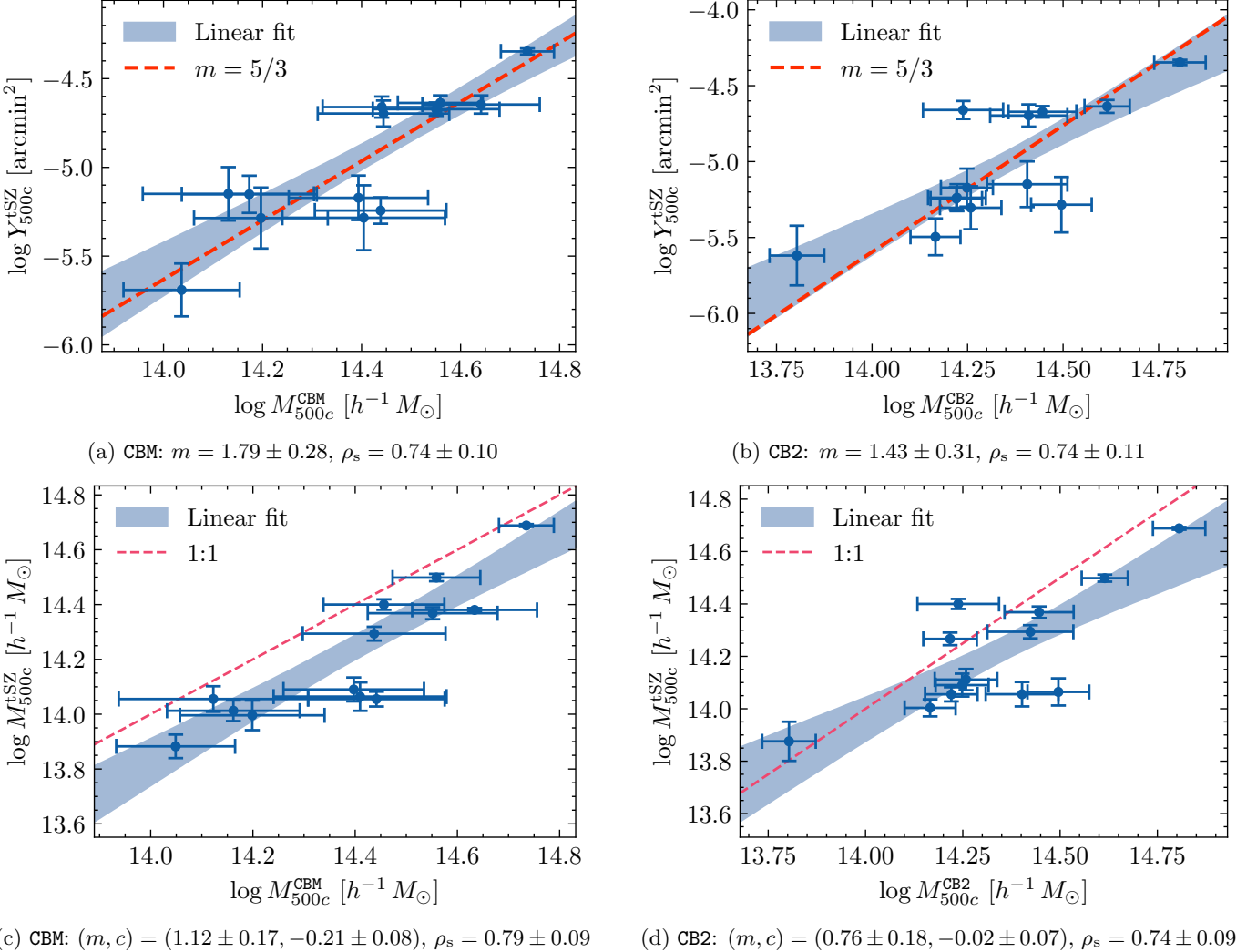


FIG. 5.— Planck cluster scaling relations. *Top row*: integrated Compton parameter Y_{500c}^{tSZ} versus BORG halo mass for which we show the expected self-similar slope of 5/3 as a red dashed line. *Bottom row*: Planck-calibrated mass M_{500c}^{tSZ} versus BORG halo mass, the one-to-one relation is shown as a red dashed line.

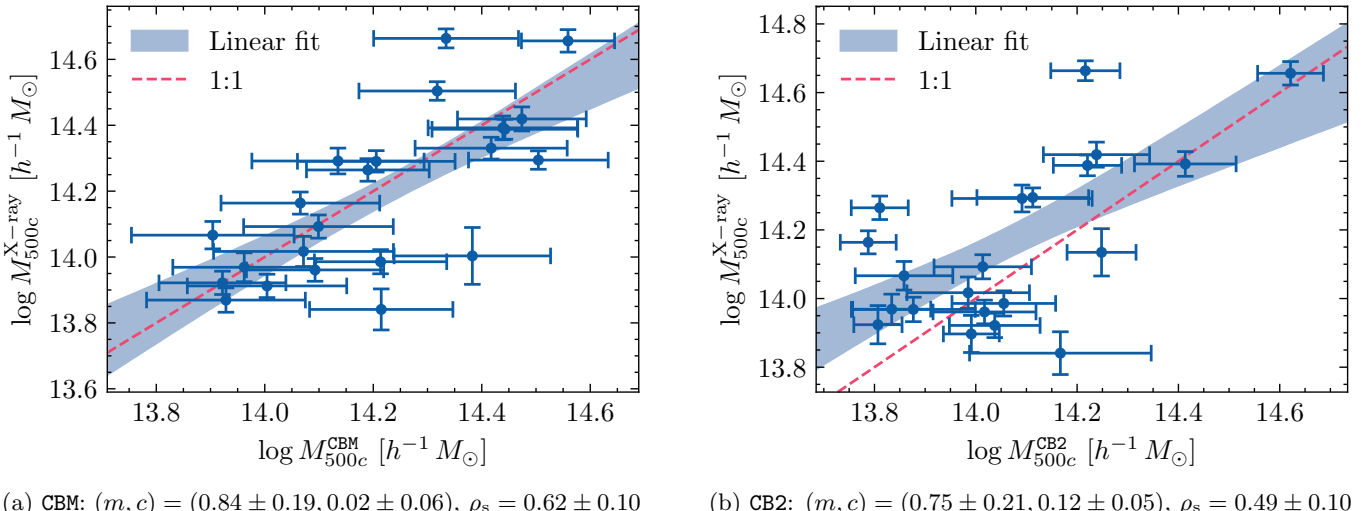


FIG. 6.— eROSITA mass-mass relations comparing $M_{500c}^{\text{X-ray}}$ to the BORG halo mass. The one-to-one relation is shown as a red dashed line.

tion *et al.* 2016d), demonstrating that constrained realisations can successfully reproduce both the location and thermodynamic imprint of local clusters in Compton- γ maps.

Subsequent efforts refined these approaches by incorporating peculiar velocity data to better constrain the large-scale gravitational field. The CLUES project (Gottlöber *et al.* 2010; Sorce *et al.* 2016) used distance indicators from the CosmicFlows programme to reduce cosmic variance on scales up to $\sim 150 h^{-1}$ Mpc, providing improved predictions for the spatial distribution of massive haloes and their associated gas. Building on this, the SLOW collaboration presented a $500 h^{-1}$ Mpc constrained hydrodynamical simulation based on CLUES initial conditions and CosmicFlows-2 velocities (Dolag *et al.* 2023; Tully *et al.* 2013). Using this framework, several studies investigated the thermodynamic properties of local clusters, including comparisons of X-ray and tSZ-derived masses (Hernández-Martínez *et al.* 2024), projection effects in Virgo (Sorce *et al.* 2021; Lebeau *et al.* 2024), and the contribution of local tSZ and kinetic Sunyaev–Zel’dovich (kSZ) signals to large-scale CMB anomalies (Jung *et al.* 2024).

These velocity-based constrained simulations provide a complementary perspective to BORG-based reconstructions, which infer initial conditions from galaxy redshift surveys such as 2M++ using a fully Bayesian forward model. Because the two approaches rely on different data and assumptions, cross-validation using observables such as the tSZ signal is essential. Indeed, Stiskalek *et al.* (2025) showed that BORG-based reconstructions reproduce peculiar velocity samples more accurately than CLUES-based initial conditions (Sorce 2018; Sorce *et al.* 2020), implying a more faithful reconstruction of the local velocity field. This improvement is reflected in cluster positions: while SLOW exhibits typical offsets of $\gtrsim 10 h^{-1}$ Mpc for well-constrained systems (Hernández-Martínez *et al.* 2024), the matching criteria adopted here correspond to spatial separations of only a few h^{-1} Mpc at low redshift, highlighting the tighter angular and positional agreement achieved by BORG-based digital twins such as CBM (see Table 3 for the separations in CBM). Our tSZ-based validation confirms this quantitatively: of the clusters in our sample (Table 1), only two SLOW counterparts achieve $p_{\text{tSZ}} < 0.05$, whereas the majority of clusters in CB2 and CBM are detected at much higher significance (Fig. 1).

5.2. Validation metrics

Our approach to quantifying the quality of the match between simulated clusters and the tSZ signal complements the LUM framework of Pfeifer *et al.* (2023), which scores reconstructions by comparing simulated and observed cluster positions in three-dimensional redshift space to associate simulated haloes with observed counterparts. While powerful, this method is complicated by uncertainties in cluster distances, which can exceed several hundred km s^{-1} even for nearby systems. By contrast, our tSZ-based test focuses on angular agreement with observed hotspots, sidestepping radial distance uncertainties entirely; the goal here is not to establish halo–cluster associations but simply to assess significance against the tSZ map. This enables the derivation of per-cluster significance values that quantify how well

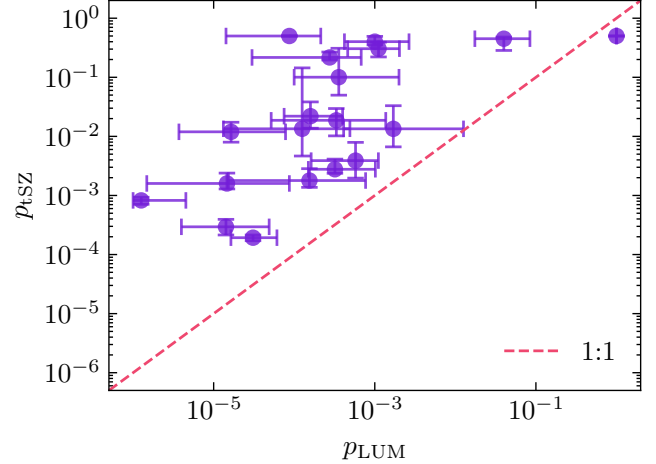


FIG. 7.— Comparison of p_{LUM} -values and p_{tSZ} -values for selected clusters (Table 1) in CBM. Points show the median p -value across realisations for each cluster, with error bars indicating the 16th–84th percentile spread. The red dashed line indicates 1:1 correspondence. The two metrics are correlated, though the tSZ test is generally stricter.

the reconstructed halo positions coincide with the thermal gas distribution on the sky. Fig. 7 compares p_{LUM} -values, computed from the probability that a halo at a given distance could produce the observed cluster position given its mass, with p_{tSZ} -values for selected clusters. The two metrics are weakly correlated, as expected since both probe positional agreement, though the tSZ test is generally stricter, yielding lower p_{tSZ} -values for clusters that are marginally significant under the LUM criterion. The large spread in p_{LUM} -values for individual clusters reflects the spatial extent of halo associations: haloes near the observed position have low p_{LUM} -values, while more distant members have high p_{LUM} -values.

Second, we derive stacked tSZ profiles centred on simulated haloes, similarly to McAlpine (2025), and compare two generations of BORG reconstructions. While sensitive to angular agreement like the per-cluster test, stacking addresses how well structures are reconstructed as a function of halo mass on average.

Third, we introduce a metric that goes beyond angular agreement to test the scaling between halo mass and the observable of an associated cluster. Even on the tSZ side, extracting the integrated Compton parameter relies on assumptions about the cluster extent, introducing model dependence. Direct mass comparisons are more complicated still: both tSZ and X-ray masses rely on external calibrations—hydrostatic equilibrium or weak lensing—each with its own systematics. Of these, weak-lensing calibration is generally more reliable, as it measures the total projected mass without assuming dynamical equilibrium.

Part of the purpose here is to build larger matched samples over which to test the mass calibration of individual clusters. This must be balanced against spurious matches, for which reason we adopt strict matching criteria of $\Delta\theta < 60'$ and $\Delta cz < 300 \text{ km s}^{-1}$ (Section 3.4). We have verified that under these criteria very few haloes from the earlier Jasche and Lavaux (2019) initial conditions in the CSIBORG1 suite (Bartlett *et al.* 2021) would be matched to observed tSZ counterparts, underscoring the improvement in reconstruction fidelity achieved by

later generations of **BORG**.

We have not yet formalised our mass-based metrics into a single Bayesian evidence; instead, we examine the inferred slope and intercept of power-law scaling relations, the intrinsic scatter, and the Spearman correlation coefficient. A proper quantification would compute the Bayesian evidence, as done for velocity field comparisons by [Stiskalek et al. \(2025\)](#). The evidence depends on both the model and the data: in the limit of independent data points, the likelihood factorises over individual cluster contributions, and the evidence is the integral of this likelihood weighted by the prior over model parameters. However, a complication arises because different simulations yield different numbers of matched clusters—for instance, one reconstruction may fail to reproduce a particular cluster entirely. A straightforward evidence comparison would therefore be ambiguous unless one also penalises local Universe models that fail to reproduce observed systems. Developing a fully probabilistic matching framework that naturally incorporates such penalties, enabling rigorous Bayesian model comparison across reconstructions, is a key direction for future work.

5.3. Future directions

Digital twins provide a complementary framework to purely statistical analyses of the tSZ signal. While standard tSZ studies extract cosmological information from ensemble statistics of the Compton- y field, digital twins retain the spatial phase information of the local density and velocity fields, enabling object-level comparisons and physically motivated interpretations. By anchoring the tSZ signal to a posterior set of large-scale structure realisations, digital twins allow explicit modelling of projection effects, cluster environments, and line-of-sight contributions that are otherwise absorbed into effective scatter or noise terms. This approach is particularly valuable in the local Universe, where cosmic variance and individual massive clusters dominate the tSZ signal, and demonstrates how digital twins can augment statistical tSZ analyses by providing additional physical context. In our case, the context is “learnt” from large-scale structure (the galaxy number density field) by the **BORG** algorithm under the assumption of the standard cosmological model.

Besides developing a full evidence comparison between different reconstructions as described above, we note three ways in which this work could be taken forward. First, incorporating tSZ or X-ray cluster data as additional likelihood terms within the **BORG** framework would improve constraints on halo masses and positions in under-sampled regions where galaxy redshift surveys provide limited information. This would improve the precision of the inferred initial conditions of the local Universe, further improving the fidelity of the reconstructions. A key technical challenge, however, is forward-modelling cluster masses within a differentiable inference pipeline, as halo identification and mass estimation are not straightforwardly differentiable operations. Recent work has demonstrated gradient-free optimisation of initial conditions using non-differentiable structure formation models that can be extended efficiently to larger volumes ([Doeser et al. 2025](#)), though extending this to full posterior sampling remains an open problem. Alternatively, differentiable halo finders have been devel-

oped ([Horowitz and Bayer 2025](#)), though discrete particle membership remains a fundamental obstacle to stable gradient propagation.

The second extension would be to use **BORG** in conjunction with the CMB to obtain new constraints on astrophysical objects. The approach here would be to forward-model Compton- y (and/or X-ray) maps using CBM cluster catalogues plus a scheme for “baryonifying” the dark matter structures by using semi-empirical or semi-analytic models for the free electron distribution, temperature and pressure profile (e.g. [Arnaud et al. 2010](#); [Battaglia et al. 2012a,b](#)). Comparing to the measurements with a pixel-by-pixel likelihood would then afford precise constraints on these baryonic parameters. This is similar to previous work constraining baryons with the tSZ signal ([Koukoufilippas et al. 2020](#); [Yan et al. 2021](#); [Tröster et al. 2022](#); [Koukoufilippas et al. 2022](#); [La Posta et al. 2025](#)), but crucially the use of constrained simulations provides the connection to dark matter on an object-by-object basis.

The final stage would be to use **BORG** to assist in modelling the CMB itself. The idea here would be to forward-model all relevant secondary anisotropies using **BORG** posterior fields to the map level—i.e. $\bar{I}_\nu(n)$ (plus polarisation in principle)—and then fit the CMB data in conjunction with CMB primary, foregrounds (which could also be informed by **BORG**) and instrumental effects. This would integrate the study of large-scale structure with study of the CMB, allowing inferences from both to be made simultaneously and explicitly self-consistently.

6. CONCLUSION

We have validated two generations of **BORG**-based constrained simulations of the local Universe—CB2 (initial conditions from [Stopyra et al. 2024](#)) and CBM (initial conditions from [McAlpine et al. 2025](#))—against *Planck* tSZ and eROSITA X-ray cluster observations. To do so, we introduced three complementary tests: per-cluster angular positioning using p_{tSZ} -values derived from the Compton- y map, stacked radial profiles as a function of halo mass, and mass scaling relations for matched cluster samples.

The majority of selected clusters are reproduced with high fidelity ($p_{\text{tSZ}} < 0.05$), with Coma, Shapley (A3558), and Perseus among the best-constrained systems. By contrast, only two clusters in **SLOW** ([Hernández-Martínez et al. 2024](#))—a hydrodynamical resimulation of CLUES velocity-constrained initial conditions ([Sorce et al. 2016](#))—achieve $p_{\text{tSZ}} < 0.05$, underscoring the superior positional accuracy of **BORG**-based digital twins. Perseus is absent in CB2 ([Stopyra et al. 2024](#)) but well reproduced in CBM ([McAlpine et al. 2025](#)). CBM yields systematically higher halo masses than CB2, in good agreement with weak-lensing-calibrated eROSITA masses as shown by [McAlpine \(2025\)](#). This demonstrates that future field-level models of the CMB informed by large-scale structure should use **BORG**—specifically its latest incarnation as **Manticore**—as their foundation.

The tSZ effect provides a powerful validation observable that complements velocity field comparisons, probing the angular positioning and masses of clusters independently of distance uncertainties. By matching simulated haloes to observed clusters, digital twins can be used to study mass calibration on a per-cluster basis,

offering an alternative to stacked weak lensing analyses.

Looking ahead, formalising these metrics into a Bayesian evidence framework would enable rigorous model comparison across reconstructions, while incorporating tSZ and X-ray cluster data as likelihood terms directly into the **BORG** inference could further improve constraints on halo masses and positions in regions where galaxy redshift surveys provide limited information. Our work also paves the way for inferring astrophysical parameters by forward-modelling Compton- y maps using **BORG**-based halo catalogues, and even more ambitiously for inferring large-scale structure and the CMB (primary, secondary and foregrounds) simultaneously and self-consistently using an integrated field-level likelihood.

ACKNOWLEDGMENTS

We thank David Alonso, Mayeul Aubin, Pedro Ferreira, Jens Jasche, and Guilhem Lavaux for useful inputs

and discussions. RS acknowledges financial support from STFC Grant No. ST/X508664/1 and the Snell Exhibition of Balliol College, Oxford. HD is supported by a Royal Society University Research Fellowship (grant no. 211046). This work was done within the Aquila Consortium⁸.

DATA AVAILABILITY

The code used in this work is available at <https://github.com/Richard-Sti/CMBOlympics>. The **Manticore** data products are available at <https://digitaletwin.fysik.su.se>. The eROSITA DR1 cluster catalogue is available at https://erosita.mpe.mpg.de/dr1/AllSkySurveyData_dr1/Catalogues.dr1/. The **Planck** PSZ2 cluster catalogue is available at <https://heasarc.gsfc.nasa.gov/w3browse/all/plancksz2.html>. The **Planck** Compton- y map was publicly released by McCarthy and Hill (2024). All other data are available upon reasonable request.

REFERENCES

R. A. Sunyaev and Y. B. Zeldovich, *Astrophysics and Space Science* **7**, 3 (1970).

R. A. Sunyaev and Y. B. Zeldovich, *Comments on Astrophysics and Space Physics* **4**, 173 (1972).

T. Mroczkowski, D. Nagai, K. Basu, J. Chluba, J. Sayers, R. Adam, E. Churazov, A. Crites, L. Di Mascolo, D. Eckert, J. Macias-Perez, F. Mayet, L. Perotto, E. Pointecouteau, C. Romero, F. Ruppin, E. Scannapieco, and J. ZuHone, *Space Science Reviews* **215**, 17 (2019), arXiv:1811.02310 [astro-ph.CO].

A. von der Linden, M. T. Allen, D. E. Applegate, P. L. Kelly, S. W. Allen, H. Ebeling, P. R. Burchat, D. L. Burke, D. Donovan, R. G. Morris, R. Blandford, T. Erben, and A. Mantz, *MNRAS* **439**, 2 (2014), arXiv:1208.0597 [astro-ph.CO].

H. Hoekstra, R. Herbonnet, A. Muzzin, A. Babul, A. Mahdavi, M. Viola, and M. Cacciato, *MNRAS* **449**, 685 (2015), arXiv:1502.01883 [astro-ph.CO].

P. Collaboration, *Astronomy & Astrophysics* **594**, A22 (2016).

L. Salvati, M. Douspis, A. Ritz, N. Aghanim, and A. Babul, *Astronomy & Astrophysics* **626**, A27 (2019).

Planck Collaboration, P. A. R. Ade, N. Aghanim, et al., *A&A* **571**, A20 (2014), arXiv:1303.5080 [astro-ph.CO].

Planck Collaboration, P. A. R. Ade, N. Aghanim, M. Arnaud, M. Ashdown, J. Aumont, C. Baccigalupi, A. J. Banday, R. B. Barreiro, J. G. Bartlett, et al., *A&A* **594**, A24 (2016a), arXiv:1502.01597 [astro-ph.CO].

T. de Haan, B. A. Benson, L. E. Bleem, S. W. Allen, D. E. Applegate, M. L. N. Ashby, M. Bautz, M. Bayliss, S. Bocquet, M. Brodwin, et al., *ApJ* **832**, 95 (2016), arXiv:1603.06522 [astro-ph.CO].

S. Bocquet, J. P. Dietrich, T. Schrabback, L. E. Bleem, M. Klein, S. W. Allen, D. E. Applegate, M. L. N. Ashby, M. Bautz, M. Bayliss, et al., *ApJ* **878**, 55 (2019), arXiv:1812.01679 [astro-ph.CO].

M. Hilton, C. Sifón, S. Naess, M. Madhavacheril, M. Oguri, E. Rozo, E. Rykoff, T. M. C. Abbott, S. Adhikari, M. Aguena, et al., *ApJS* **253**, 3 (2021), arXiv:2009.11043 [astro-ph.CO].

S. Bocquet, S. Grandis, L. E. Bleem, M. Klein, J. J. Mohr, T. Schrabback, J. P. Dietrich, B. Hernandez-Martin, A. Sommer, M. Aguena, et al., *Physical Review D* **110**, 083509 (2024a), arXiv:2310.12213 [astro-ph.CO].

S. Bocquet, S. Grandis, L. E. Bleem, M. Klein, J. J. Mohr, T. Schrabback, J. P. Dietrich, B. Hernandez-Martin, A. Sommer, M. Aguena, et al., *Physical Review D* **110**, 083510 (2024b), arXiv:2401.02075 [astro-ph.CO].

Planck Collaboration, N. Aghanim, M. Arnaud, et al., *A&A* **594**, A22 (2016b), arXiv:1502.01596 [astro-ph.CO].

J. Chandran, M. Remazeilles, and R. B. Barreiro, *MNRAS* **526**, 5682 (2023), arXiv:2305.10193 [astro-ph.CO].

F. McCarthy and J. C. Hill, *Phys. Rev. D* **109**, 023528 (2024), arXiv:2307.01043 [astro-ph.CO].

N. Koukoufilippas, D. Alonso, M. Bilicki, and J. A. Peacock, *MNRAS* **491**, 5464 (2020), arXiv:1909.09102 [astro-ph.CO].

Z. Yan, L. van Waerbeke, T. Tröster, A. H. Wright, D. Alonso, M. Asgari, M. Bilicki, T. Erben, S. Gu, C. Heymans, H. Hildebrandt, G. Hinshaw, N. Koukoufilippas, A. Kannawadi, K. Kuijken, A. Mead, and H. Shan, *A&A* **651**, A76 (2021), arXiv:2102.07701 [astro-ph.CO].

T. Tröster, A. J. Mead, C. Heymans, Z. Yan, D. Alonso, M. Asgari, M. Bilicki, A. Dvornik, H. Hildebrandt, B. Joachimi, A. Kannawadi, K. Kuijken, P. Schneider, H. Y. Shan, L. van Waerbeke, and A. H. Wright, *A&A* **660**, A27 (2022), arXiv:2109.04458 [astro-ph.CO].

N. Koukoufilippas, D. Alonso, M. Bilicki, and J. A. Peacock, *Monthly Notices of the Royal Astronomical Society* (2022), arXiv:1909.09102 [astro-ph.CO].

A. La Posta, D. Alonso, N. E. Chisari, T. Ferreira, and C. García-García, *Physical Review D* **112**, 043525 (2025).

N. Battaglia, J. R. Bond, C. Pfrommer, and J. L. Sievers, *ApJ* **758**, 74 (2012a), arXiv:1109.3709 [astro-ph.CO].

K. Dolag, D. Grasso, V. Springel, and I. Tkachev, *J. Cosmology Astropart. Phys.* **2005**, 009 (2005), arXiv:astro-ph/0410419 [astro-ph].

S. Gottlöber, Y. Hoffman, and G. Yepes, in *High Performance Computing in Science and Engineering, Garching/Munich 2009*, edited by S. Wagner, M. Steinmetz, A. Bode, and M. M. Müller (2010) pp. 309–322, arXiv:1005.2687 [astro-ph.CO].

J. G. Sorce, S. Gottlöber, G. Yepes, Y. Hoffman, H. M. Courtois, M. Steinmetz, R. B. Tully, D. Pomarède, and E. Carles, *MNRAS* **455**, 2078 (2016), arXiv:1510.04900 [astro-ph.CO].

J. Jasche and B. D. Wandelt, *MNRAS* **432**, 894 (2013), arXiv:1203.3639 [astro-ph.CO].

G. Lavaux and M. J. Hudson, *MNRAS* **416**, 2840 (2011), arXiv:1105.6107 [astro-ph.CO].

J. Jasche, F. Leclercq, and B. D. Wandelt, *J. Cosmology Astropart. Phys.* **2015**, 036 (2015), arXiv:1409.6308 [astro-ph.CO].

G. Lavaux and J. Jasche, *MNRAS* **455**, 3169 (2016), arXiv:1509.05040 [astro-ph.CO].

F. Leclercq, J. Jasche, G. Lavaux, B. Wandelt, and W. Percival, *J. Cosmology Astropart. Phys.* **2017**, 049 (2017), arXiv:1601.00093 [astro-ph.CO].

J. Jasche and G. Lavaux, *A&A* **625**, A64 (2019), arXiv:1806.11117 [astro-ph.CO].

G. Lavaux, J. Jasche, and F. Leclercq, arXiv e-prints, arXiv:1909.06396 (2019), arXiv:1909.06396 [astro-ph.CO].

N. Porqueres, D. Kodi Ramanah, J. Jasche, and G. Lavaux, *A&A* **624**, A115 (2019), arXiv:1812.05113 [astro-ph.CO].

⁸ <https://aquila-consortium.org>

S. Stopyra, H. V. Peiris, A. Pontzen, J. Jasche, and G. Lavaux, *MNRAS* **527**, 1244 (2024), arXiv:2304.09193 [astro-ph.CO].

S. McAlpine, arXiv e-prints , arXiv:2510.16574 (2025), arXiv:2510.16574 [astro-ph.CO].

D. J. Bartlett, H. Desmond, and P. G. Ferreira, *Phys. Rev. D* **103**, 023523 (2021), arXiv:2010.05811 [astro-ph.CO].

S. Tassev, M. Zaldarriaga, and D. J. Eisenstein, *J. Cosmology Astropart. Phys.* **2013**, 036 (2013), arXiv:1301.0322 [astro-ph.CO].

V. Springel, R. Pakmor, O. Zier, and M. Reinecke, *MNRAS* **506**, 2871 (2021), arXiv:2010.03567 [astro-ph.IM].

Planck Collaboration, N. Aghanim, Y. Akrami, *et al.*, *A&A* **641**, A1 (2020a), arXiv:1807.06205 [astro-ph.CO].

R. Stiskalek, H. Desmond, J. Devriendt, A. Slyz, G. Lavaux, M. J. Hudson, D. J. Bartlett, and H. M. Courtois, *MNRAS* (2025), 10.1093/mnras/staf1960, arXiv:2502.00121 [astro-ph.CO].

S. McAlpine, J. Jasche, M. Ata, G. Lavaux, R. Stiskalek, C. S. Frenk, and A. Jenkins, *MNRAS* **540**, 716 (2025), arXiv:2505.10682 [astro-ph.CO].

T. M. C. Abbott, M. Aguena, A. Alarcon, S. Allam, O. Alves, A. Amon, F. Andrade-Oliveira, J. Annis, S. Avila, D. Bacon, *et al.*, *Phys. Rev. D* **105**, 023520 (2022), arXiv:2105.13549 [astro-ph.CO].

Planck Collaboration, P. A. R. Ade, N. Aghanim, *et al.*, *A&A* **594**, A27 (2016c), arXiv:1502.01598 [astro-ph.CO].

R. Piffaretti, M. Arnaud, G. W. Pratt, E. Pointecouteau, and J.-B. Melin, *A&A* **534**, A109 (2011), arXiv:1007.1916 [astro-ph.CO].

M. Arnaud, G. W. Pratt, R. Piffaretti, H. Böhringer, J. H. Croston, and E. Pointecouteau, *A&A* **517**, A92 (2010), arXiv:0910.1234 [astro-ph.CO].

Planck Collaboration, P. A. R. Ade, N. Aghanim, M. Arnaud, M. Ashdown, J. Aumont, C. Baccigalupi, A. Balbi, A. J. Banday, R. B. Barreiro, *et al.*, *A&A* **536**, A8 (2011), arXiv:1101.2024 [astro-ph.CO].

M. Sereno, G. Covone, L. Izzo, S. Ettori, J. Coupon, and M. Lieu, *MNRAS* **472**, 1946 (2017), arXiv:1703.06886 [astro-ph.CO].

Planck Collaboration, N. Aghanim, Y. Akrami, M. Ashdown, J. Aumont, C. Baccigalupi, M. Ballardini, A. J. Banday, R. B. Barreiro, N. Bartolo, *et al.*, *A&A* **641**, A6 (2020b), arXiv:1807.06209 [astro-ph.CO].

E. Bulbul, A. Liu, M. Kluge, X. Zhang, J. S. Sanders, Y. E. Bahar, V. Ghirardini, E. Artis, R. Seppi, C. Garrel, M. E. Ramos-Ceja, J. Comparat, F. Balzer, K. Böckmann, M. Brüggen, N. Clerc, K. Dennerl, K. Dolag, M. Freyberg, S. Grandis, D. Gruen, F. Kleinebreit, S. Krippendorf, G. Lamer, A. Merloni, K. Migkas, K. Nandra, F. Pacaud, P. Predehl, T. H. Reiprich, T. Schrabback, A. Veronica, J. Weller, and S. Zelmer, *A&A* **685**, A106 (2024), arXiv:2402.08452 [astro-ph.CO].

P. Predehl *et al.*, *A&A* **647**, A1 (2021), arXiv:2010.03477 [astro-ph.HE].

N. T. Nguyen-Dang, N. Ota, N. Okabe, M. Oguri, I. Mitsuishi, T. H. Reiprich, F. Pacaud, E. Bulbul, J. S. Sanders, M. Brüggen, *et al.*, arXiv e-prints , arXiv:2512.06138 (2024), arXiv:2512.06138 [astro-ph.CO].

S. Grandis, V. Ghirardini, S. Bocquet, C. Garrel, J. J. Mohr, M. Kluge, E. Bulbul, N. Clerc, J. Comparat, D. Gruen, and others, *A&A* **687**, A178 (2024), arXiv:2402.08455 [astro-ph.CO].

G. O. Abel, *ApJS* **3**, 211 (1958).

K. M. Górska, E. Hivon, A. J. Banday, B. D. Wandelt, F. K. Hansen, M. Reinecke, and M. Bartelmann, *ApJ* **622**, 759 (2005), arXiv:astro-ph/0409513 [astro-ph].

A. Zonca, L. Singer, D. Lenz, M. Reinecke, C. Rosset, E. Hivon, and K. Gorski, *The Journal of Open Source Software* **4**, 1298 (2019).

S. Pfeifer, A. Valade, S. Gottlöber, Y. Hoffman, N. I. Libeskind, and W. A. Hellwing, *MNRAS* **523**, 5985 (2023), arXiv:2305.05694 [astro-ph.CO].

B. Diemer, *ApJS* **239**, 35 (2018), arXiv:1712.04512 [astro-ph.CO].

J. Tinker, A. V. Kravtsov, A. Klypin, K. Abazajian, M. Warren, G. Yepes, S. Gottlöber, and D. E. Holz, *ApJ* **688**, 709 (2008), arXiv:0803.2706 [astro-ph].

M. D. Hoffman and A. Gelman, arXiv e-prints , arXiv:1111.4246 (2011), arXiv:1111.4246 [stat.CO].

D. Phan, N. Pradhan, and M. Jankowiak, arXiv e-prints , arXiv:1912.11554 (2019), arXiv:1912.11554 [stat.ML].

E. Bingham, J. P. Chen, M. Jankowiak, F. Obermeyer, N. Pradhan, T. Karaletsos, R. Singh, P. Szerlip, P. Horsfall, and N. D. Goodman, *Journal of Machine Learning Research* **20**, 1 (2019).

A. Gelman and D. B. Rubin, *Statistical Science* **7**, 457 (1992).

N. Kaiser, *MNRAS* **222**, 323 (1986).

A. C. Fabian, J. S. Sanders, G. B. Taylor, S. W. Allen, C. S. Crawford, R. M. Johnstone, and K. Iwasawa, *MNRAS* **366**, 417 (2006), arXiv:astro-ph/0510476 [astro-ph].

C. P. Haines, G. Busarello, P. Merluzzi, K. A. Pimbblet, F. P. A. Vogt, M. A. Dopita, A. Mercurio, A. Grado, and L. Limatola, *MNRAS* **481**, 1055 (2018), arXiv:1807.11525 [astro-ph.CO].

Y. Higuchi, N. Okabe, P. Merluzzi, C. P. Haines, G. Busarello, A. Grado, and A. Mercurio, *MNRAS* **497**, 52 (2020), arXiv:2006.08130 [astro-ph.CO].

M. Rossetti, S. Ghizzardi, S. Molendi, and A. Finoguenov, *A&A* **463**, 839 (2007), arXiv:astro-ph/0611056 [astro-ph].

M. S. Mirakhor, S. A. Walker, M. Sundquist, and D. Chandra, *MNRAS* **526**, L124 (2023), arXiv:2308.16222 [astro-ph.CO].

S. Bardelli, E. Zucca, G. Zamorani, G. Vettolani, and R. Scaramella, *MNRAS* **296**, 599 (1998), arXiv:astro-ph/9712218 [astro-ph].

R. Monteiro-Oliveira, D. F. Morell, V. M. Sampaio, A. L. B. Ribeiro, and R. R. de Carvalho, *MNRAS* **509**, 3470 (2022), arXiv:2111.03053 [astro-ph.CO].

E. Hernández-Martínez, K. Dolag, B. Seidel, J. G. Sorce, N. Aghanim, S. Pilipenko, S. Gottlöber, T. Lebeau, and M. Valentini, *A&A* **687**, A253 (2024), arXiv:2402.01834 [astro-ph.CO].

D. J. Bartlett and H. Desmond, *The Open Journal of Astrophysics* **6**, 42 (2023), arXiv:2309.00948 [stat.ME].

Planck Collaboration, P. A. R. Ade, N. Aghanim, *et al.*, *A&A* **596**, A101 (2016d), arXiv:1511.05156 [astro-ph.CO].

K. Dolag, J. G. Sorce, S. Pilipenko, E. Hernández-Martínez, M. Valentini, S. Gottlöber, N. Aghanim, and I. Khabibullin, *A&A* **677**, A169 (2023), arXiv:2302.10960 [astro-ph.CO].

R. B. Tully, H. M. Courtois, A. E. Dolphin, J. R. Fisher, P. Héraudeau, B. A. Jacobs, I. D. Karachentsev, D. Makarov, L. Makarova, S. Mitronova, L. Rizzi, E. J. Shaya, J. G. Sorce, and P.-F. Wu, *AJ* **146**, 86 (2013), arXiv:1307.7213 [astro-ph.CO].

J. G. Sorce, Y. Dubois, J. Blaizot, S. L. McGee, G. Yepes, and A. Knebe, *MNRAS* **504**, 2998 (2021), arXiv:2104.13389 [astro-ph.CO].

T. Lebeau, J. G. Sorce, N. Aghanim, E. Hernández-Martínez, and K. Dolag, *A&A* **682**, A157 (2024), arXiv:2310.02326 [astro-ph.CO].

G. Jung, N. Aghanim, J. G. Sorce, B. Seidel, K. Dolag, and M. Douspis, *A&A* **692**, A180 (2024), arXiv:2406.11543 [astro-ph.CO].

J. G. Sorce, *MNRAS* **478**, 5199 (2018), arXiv:1806.09633 [astro-ph.CO].

J. G. Sorce, H. M. Courtois, S. Gottlöber, Y. Hoffman, and R. B. Tully, *MNRAS* **495**, 4463 (2020), arXiv:2005.08074 [astro-ph.CO].

L. Doeser, M. Ata, and J. Jasche, *MNRAS* **542**, 1403 (2025), arXiv:2502.13243 [astro-ph.CO].

B. Horowitz and A. E. Bayer, arXiv e-prints , arXiv:2510.26851 (2025), arXiv:2510.26851 [astro-ph.IM].

N. Battaglia, J. R. Bond, C. Pfrommer, and J. L. Sievers, *ApJ* **758**, 75 (2012b), arXiv:1109.3711 [astro-ph.CO].

APPENDIX

A. SCALING RELATION FITS

Table 2 summarises the fitted scaling relation parameters for both observable-mass and mass-mass relations.

We fit relations of the form $\log Y = m \log M + c$ with intrinsic scatter σ_{int} , where Y is either the catalogue observable or catalogue mass, and M is the matched BORG halo mass. The Spearman correlation coefficient ρ_s quantifies the strength of the correlation, while τ_m and $\tau_{m,c}$

give the tension with the self-similar slope ($m = 4/3$ for X-ray luminosity, $m = 5/3$ for tSZ; [Kaiser 1986](#)) and unity relation ($m = 1$, $c = 0$), respectively.

B. CLUSTER SAMPLE PROPERTIES

Fig. 8 shows the fraction of observed clusters matched to halo associations as a function of catalogue-reported mass; higher-mass clusters are more likely to have counterparts in both simulations. Table 3 summarises the

properties of the selected nearby clusters (Section 2.5) and their matched halo associations in CB2 and CBM.

This paper was built using the Open Journal of Astrophysics L^AT_EX template. The OJA is a journal which provides fast and easy peer review for new papers in the `astro-ph` section of the arXiv, making the reviewing process simpler for authors and referees alike. Learn more at <http://astro.theoj.org>.

Observable–mass scaling relations						
Catalogue	Simulation	m	c	σ_{int}	ρ_s	τ_m
eROSITA	CB2	1.39 ± 0.34	1.46 ± 0.08	0.30 ± 0.06	0.51 ± 0.09	0.2σ
	CBM	1.63 ± 0.34	1.26 ± 0.10	0.21 ± 0.08	0.63 ± 0.10	0.9σ
Planck	CB2	1.43 ± 0.31	-1.51 ± 0.13	0.22 ± 0.10	0.74 ± 0.11	0.8σ
	CBM	1.79 ± 0.28	-1.73 ± 0.15	0.08 ± 0.07	0.74 ± 0.10	0.4σ
Mass–mass relations						
Catalogue	Simulation	m	c	σ_{int}	ρ_s	$\tau_{m,c}$
eROSITA	CB2	0.75 ± 0.21	0.12 ± 0.05	0.18 ± 0.04	0.49 ± 0.10	2.1σ
	CBM	0.84 ± 0.19	0.02 ± 0.06	0.14 ± 0.04	0.62 ± 0.10	0.5σ
Planck	CB2	0.76 ± 0.18	-0.02 ± 0.07	0.14 ± 0.04	0.74 ± 0.09	2.2σ
	CBM	1.12 ± 0.17	-0.21 ± 0.08	0.05 ± 0.04	0.79 ± 0.09	4.7σ

TABLE 2

SCALING RELATION FITS OF THE FORM $\log Y = m \log M + c$, WHERE M IS IN UNITS OF $10^{14} h^{-1} M_\odot$. *Top*: OBSERVABLE–MASS RELATIONS, WHERE Y IS $L_{500c}^{\text{X-ray}}$ IN UNITS OF $10^{44} \text{ ergs}^{-1}$ (eROSITA) OR Y_{500c}^{tSZ} IN UNITS OF 10^{-4} Mpc^2 (PLANCK); τ_m GIVES THE TENSION WITH THE SELF-SIMILAR EXPECTATION ($m = 4/3$ FOR X-RAY, $m = 5/3$ FOR TSZ). *Bottom*: MASS–MASS RELATIONS COMPARING CATALOGUE M_{500c} TO BORG HALO MASSES, BOTH IN UNITS OF $10^{14} h^{-1} M_\odot$; $\tau_{m,c}$ GIVES THE JOINT TENSION WITH THE ONE-TO-ONE RELATION ($m = 1$, $c = 0$).

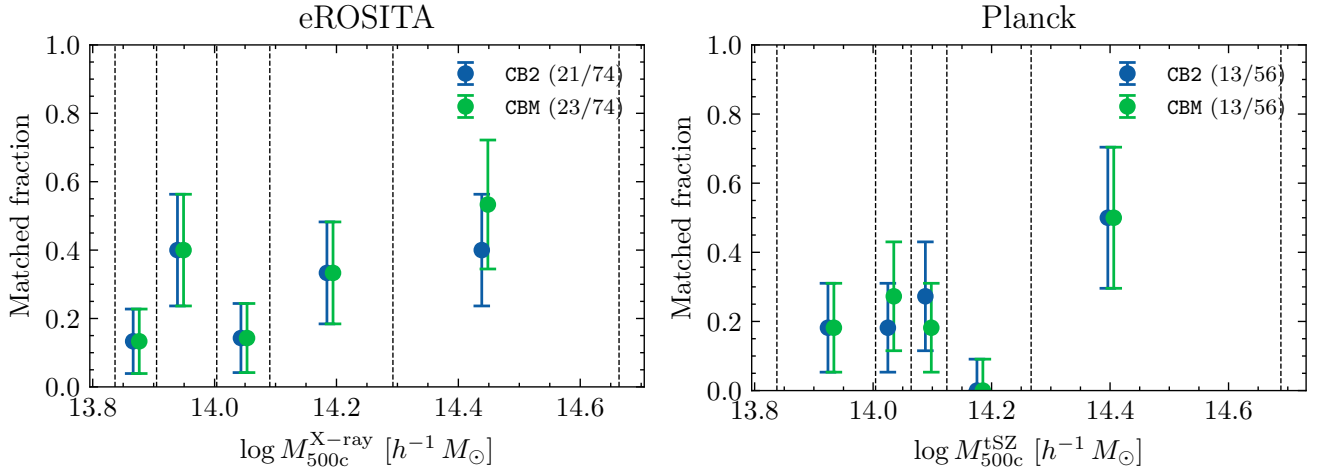


FIG. 8.— Fraction of observed clusters matched to halo associations as a function of catalogue-reported mass M_{500c} for eROSITA (left) and Planck (right). Clusters are divided into percentile bins above $M_{500c} = 10^{14} h^{-1} M_\odot$, with vertical dashed lines indicating bin edges. Error bars show Poisson uncertainties. The total matched fractions are indicated in the legend. Higher-mass clusters are more likely to be matched, with approximately half of the most massive clusters having counterparts in both simulations.

CB2								
Cluster	d [h^{-1} Mpc]	3D sep [h^{-1} Mpc]	ℓ [deg]	b [deg]	f_{present}	$\log M_{500c}$ [$h^{-1} M_{\odot}$]	p_{LUM}	\tilde{p}_{tSZ}
Virgo	10.5	3.1	291.6	74.7	0.80	13.97	5.3×10^{-3}	4.7×10^{-3}
Centaurus (A3526)	33.1	2.3	302.9	21.2	0.85	13.82	4.1×10^{-3}	1.2×10^{-1}
Hydra (A1060)	41.1	1.6	269.8	26.5	1.00	14.09	5.1×10^{-4}	2.3×10^{-1}
Norma (A3627)	48.8	4.1	325.5	-7.5	0.85	13.88	2.1×10^{-2}	—
Perseus (A426)	—	—	—	—	—	—	—	—
Leo (A1367)	63.3	1.6	234.2	73.3	1.00	14.22	3.2×10^{-4}	6.0×10^{-3}
Coma (A1656)	70.9	2.4	61.5	88.3	1.00	14.82	4.5×10^{-5}	2.4×10^{-4}
Hercules (A2199)	94.4	3.0	63.4	43.8	1.00	14.31	1.1×10^{-3}	5.6×10^{-3}
Abell 496	96.8	0.8	209.1	-36.6	0.95	14.21	3.8×10^{-5}	2.0×10^{-2}
Hercules (A2063)	102.8	1.1	12.7	49.5	1.00	14.26	1.1×10^{-4}	3.8×10^{-2}
Hercules (A2151)	—	—	—	—	—	—	—	—
Hercules (A2147)	108.2	3.6	30.6	44.3	1.00	14.55	7.6×10^{-4}	9.1×10^{-3}
Shapley (A3571)	114.3	1.4	316.5	28.7	0.95	14.61	3.1×10^{-5}	1.8×10^{-3}
Abell 548	120.3	4.5	230.2	-24.5	1.00	14.08	1.1×10^{-2}	3.8×10^{-1}
Abell 119	125.8	2.4	125.5	-64.1	1.00	14.44	4.5×10^{-4}	1.4×10^{-3}
Abell 1736	136.2	3.0	312.8	35.0	0.95	14.41	9.0×10^{-4}	5.2×10^{-3}
Abell 1644	139.2	0.5	305.0	45.3	1.00	14.25	1.4×10^{-5}	3.3×10^{-3}
Shapley (A3558)	144.0	0.8	312.3	30.6	1.00	14.93	6.4×10^{-7}	6.9×10^{-4}
CBM								
Cluster	d [h^{-1} Mpc]	3D sep [h^{-1} Mpc]	ℓ [deg]	b [deg]	f_{present}	$\log M_{500c}$ [$h^{-1} M_{\odot}$]	p_{LUM}	\tilde{p}_{tSZ}
Virgo	13.1	1.8	288.4	73.3	0.96	14.24	5.8×10^{-4}	3.9×10^{-3}
Centaurus (A3526)	34.1	2.3	302.8	21.6	0.96	14.20	1.1×10^{-3}	3.0×10^{-1}
Hydra (A1060)	43.4	1.3	269.6	26.4	1.00	14.18	2.8×10^{-4}	2.2×10^{-1}
Norma (A3627)	51.2	2.0	325.3	-6.3	0.96	14.66	8.7×10^{-5}	—
Perseus (A426)	51.2	1.5	150.3	-13.5	1.00	14.75	1.4×10^{-5}	2.9×10^{-4}
Leo (A1367)	66.7	0.6	233.4	73.2	0.98	14.44	1.6×10^{-5}	1.2×10^{-2}
Coma (A1656)	72.2	1.8	62.3	88.2	1.00	14.74	3.1×10^{-5}	1.9×10^{-4}
Hercules (A2199)	94.3	3.0	63.4	43.7	1.00	14.68	1.6×10^{-4}	2.2×10^{-2}
Abell 496	100.7	2.0	209.4	-36.5	0.88	14.37	3.3×10^{-4}	1.9×10^{-2}
Hercules (A2063)	100.6	1.6	12.3	49.5	0.96	14.28	3.6×10^{-4}	1.0×10^{-1}
Hercules (A2151)	118.5	5.8	32.1	44.2	0.54	13.94	4.0×10^{-2}	4.5×10^{-1}
Hercules (A2147)	106.0	3.3	29.9	44.4	0.94	14.63	3.2×10^{-4}	2.8×10^{-3}
Shapley (A3571)	113.6	0.8	316.5	28.6	1.00	14.57	1.5×10^{-5}	1.6×10^{-3}
Abell 548	117.8	3.9	230.4	-25.0	0.90	14.52	1.0×10^{-3}	4.0×10^{-1}
Abell 119	125.3	2.1	125.5	-63.8	0.96	14.58	1.5×10^{-4}	1.8×10^{-3}
Abell 1736	136.5	4.3	312.4	34.9	0.84	14.45	1.7×10^{-3}	1.3×10^{-2}
Abell 1644	140.5	1.0	305.0	45.3	0.72	14.46	1.3×10^{-4}	1.3×10^{-2}
Shapley (A3558)	145.5	1.4	312.2	30.6	0.90	15.07	1.3×10^{-6}	8.2×10^{-4}

TABLE 3

PROPERTIES OF THE SELECTED CLUSTERS AND THEIR MATCHED HALO ASSOCIATIONS FOR CB2 (TOP) AND CBM (BOTTOM). WE REPORT THE COMOVING DISTANCE d TO THE MATCHED HALO ASSOCIATION, 3D SEPARATION (3D SEP) BETWEEN THE OBSERVED AND SIMULATED CLUSTER POSITIONS, GALACTIC COORDINATES (ℓ, b), ASSOCIATION PRESENCE FRACTION f_{present} , MEAN LOGARITHMIC HALO MASS $\log M$, THE LUM p -VALUE p_{LUM} QUANTIFYING MATCH SIGNIFICANCE, AND THE MEDIAN TSZ p -VALUE \tilde{p}_{tSZ} ACROSS REALISATIONS. CLUSTERS WITHOUT A MATCHED ASSOCIATION ARE MARKED WITH DASHES.